

The Effects of Atmospheric and Lateral Buoyancy Fluxes on Labrador Sea Mixed Layer Depth

Laura C. Gillard^{a,b,*}, Clark Pennelly^a, Helen L. Johnson^c, Paul G. Myers^a

^a*Department of Earth and Atmospheric Sciences, University of Alberta, Edmonton, Alberta, Canada*

^b*Center for Earth Observation Science, University of Manitoba, Winnipeg, Manitoba, Canada*

^c*Department of Earth Sciences, University of Oxford, Oxford, England*

Abstract

The depth of the Labrador Sea mixed layer during winter convection is a balance between atmospheric buoyancy loss and lateral buoyancy exchange, and is notoriously difficult to represent accurately in ocean and climate models. This study shows that lateral exchanges of heat and salt between the shelf and the interior are smaller in a regional coupled ocean-sea ice model at higher vertical resolution (75 levels compared with 50 levels), due in part to altered bathymetry along the Greenland shelf. Reduced lateral exchange results in a stronger stratification in the interior of the Labrador Sea, with stronger convection resistance which results in unrealistically shallow mixed layers. The westward fluxes of heat and salt associated with Irminger Water at Cape Farewell are 50 % and 33 % lower, respectively, with higher vertical resolution. Exchanges south of the Labrador Sea from the North Atlantic Current are also smaller, contributing to a reduction in salt and heat import into the Labrador Sea interior. When the high resolution model is forced with a stronger wintertime buoyancy loss at the ocean surface, this weakens the Labrador Sea stratification, allowing the forcing to break through the freshwater cap and increasing convection, bringing mixed layer depths back to observed values. A strong atmospheric forcing can therefore compensate for a reduction in lateral advection. The mixed layer depths, which

*Corresponding author

Email address: gillard2@ualberta.ca (Laura C. Gillard)

are representative of convection and Labrador Sea water formation, will be the focus in this study. Therefore, this study suggests that convection and Labrador Sea Water formation is a complex interplay of surface and lateral fluxes, linked to stratification thresholds.

Keywords: Numerical modelling, Labrador Sea, Oceanic convection, Sea-air exchanges, Horizontal advection, Vertical Resolution

1. Introduction

The Labrador Sea is a high-latitude partially enclosed basin of the North Atlantic Ocean. Located between Canada and Greenland and exposed to the mid-latitude storm track (Lau, 1988), winter storms, extreme winds and cold
5 temperatures drive intense heat exchange between the atmosphere and the ocean (Marshall et al., 1998). Winter buoyancy loss to the atmosphere drives deep mixing of the water column (convection) through plumes sinking to 1500 m or more (Yashayaev and Loder, 2017). After convection, the basin interior is restratified by a lateral exchange of heat and freshwater. The product of
10 convection is the Labrador Sea Water (LSW) which is exported at depth through the North Atlantic Ocean (Talley et al., 2003).

The Atlantic Meridional Overturning Circulation (AMOC) is a large-scale, 3D system of ocean currents and a crucial component of the Earth's climate system due to its role in the uptake and redistribution of heat and other climat-
15 ically important tracers. The importance of LSW formation in determining the variability and strength of the AMOC has been shown in numerous ocean modelling (e.g. Bailey et al., 2005; Feucher et al., 2019) and climate modelling (e.g. Kuhlbrodt et al., 2007) studies. A recent 21-month time series associated with the Overturning in the Subpolar North Atlantic Program (OSNAP) observing
20 system suggested that the eastern sub-polar gyre, rather than the Labrador Sea, was largely responsible for setting the strength of the overturning in the sub-polar North Atlantic (Lozier et al., 2019; Petit et al., 2020). The LSW formation provides the densest component of the Subpolar Mode Water due to

the air-sea and lateral heat exchange as the Subpolar Mode Water is advected
25 around the cyclonic current system in the Subpolar North Atlantic (McCartney
and Talley, 1982). Regardless of the Labrador Sea’s role in AMOC variability,
LSW formation is still a crucial process for the ventilation of the deep ocean,
transporting heat, nutrients, oxygen, and carbon dioxide from the surface layers
to depth (Rhein et al., 2017; MacGilchrist et al., 2020). As MacGilchrist et al.
30 (2020) shows, there is an important distinction between deep water formation
and ventilation and the regions where they occur. Therefore, the processes that
control deep water formation in the Labrador Sea are important to understand.

Many factors are important for deep convection in the Labrador Sea, such
as Arctic freshwater export, storm tracks, and air temperature (Våge et al.,
35 2009); therefore, understanding the mechanisms for initiating deep convection
is complicated. Shifts in storm tracks can influence the convection, as strong
westerlies off eastern Canada drag cold air over the Labrador Sea. Frequency
and intensity of storms play a major role in the heat loss in the Labrador Sea
(Våge et al., 2009; Schulze et al., 2016). Cold air temperatures over an open
40 ocean can increase the heat exchange from the ocean to the air, decreasing the
temperature at the surface and thereby increasing the density and initiating
deep convection (Våge et al., 2009). Anomalous cold atmospheric conditions
over the Labrador Sea, which intensify convection, can impact the variability of
the LSW on interannual to decadal time scales (Rhein et al., 2017).

45 The Labrador Sea is restratified by the lateral transport of buoyant waters
from the boundary currents to the interior. The West Greenland Current, a
boundary current that flows along the west coast of Greenland, carries cold and
fresh waters along the surface, above warmer and saltier waters from Irminger
Sea (~ 200 -500 m depth; Cuny et al., 2002). The water column of the interior
50 of the Labrador Sea is warmed, and its salinity is modified through lateral
fluxes from the warm, salty, subsurface Irminger Water as well as from the
fresh surface boundary currents (Straneo, 2006; Yashayaev and Loder, 2009).
The subsurface warming produces a flux of heat and salt into the surface layers
in the Labrador Sea (Straneo, 2006). The surface boundary currents contain

55 freshwater fluxes from the Arctic, as well as the Greenland Ice Sheet's (GrIS) meltwater (Dukhovskoy et al., 2019).

In the last decade, there has been an increase in freshwater content in the Arctic Ocean (Rabe et al., 2014), an increase in southward freshwater export via Fram Strait (de Steur et al., 2018) and an increase in the GrIS freshwa-
60 ter flux (Bamber et al., 2018). Observational and modelling studies suggest that the Labrador Sea's convection has not yet been impacted by the input of GrIS meltwater (Böning et al., 2016; Rhein et al., 2018; Yashayaev and Loder, 2017; Dukhovskoy et al., 2019); although, model studies have suggested that the GrIS freshwater flux may enter the interior of the Labrador Sea (Böning et al.,
65 2016; Gillard et al., 2016; Luo et al., 2016). Therefore, freshwater anomalies in the Labrador Sea boundary currents in recent years likely include a signal of increased export of Polar Water and GrIS meltwater (Dukhovskoy et al., 2019).

The Labrador Sea convection strength can weaken due to an increase of buoyant waters in the interior of the Labrador Sea in combination with a weak
70 atmospheric forcing (weak winds and mild winters). Wind-driven Ekman transport and eddies transport freshwater from the surface boundary currents along the Greenland shelf and into the basin (Schulze Chretien and Frajka-Williams, 2018; Luo et al., 2016). Eddies, from the boundary currents, try to restratify after convection by flattening the density gradients to reach a stable water col-
75 umn. There exists different types of eddies observed near the Labrador Sea. A specific type of eddy, Irminger Rings, contribute to the restratification of the Labrador Sea with their warm salty water at depth and cold fresh surface water (de Jong et al., 2014; Gelderloos et al., 2011; Katsman et al., 2004). They are the largest and most energetic type of eddy in this region (11 - 35 km radius),
80 generated by the barotropic instability of the West Greenland and Irminger Currents off Cape Desolation (Chanut et al., 2008). The other two types of eddy in this region, convective eddies and boundary current eddies, are smaller, on the order of the baroclinic Rossby deformation radius (about 7 km in the Labrador Sea), and therefore harder for models to resolve. Boundary current eddies play
85 a small role in re-stratifying the region (de Jong et al., 2014; Gelderloos et al.,

2011; Chanut et al., 2008; Katsman et al., 2004). The relative importance of convective eddies is still debated (Rieck et al., 2019).

To complicate the understanding of the Labrador Sea convection, the ocean’s convection cycle has a memory, with a preconditioning stage which acts as a
90 positive feedback (Schulze et al., 2016; Yashayaev and Loder, 2017). Years with weak convection or large freshwater fluxes into the Labrador Sea create a buoyant cap that makes it harder for heat loss occurring at the surface to break this barrier and initiate convection in subsequent years. The opposite is true as well, as years with relatively strong convection results in such a well-mixed
95 water column that during the following convective season the water column is preconditioned to convect easily. Therefore, lateral exchanges of heat and freshwater by wind forcing (Ekman transport) and eddies combine with air-sea heat fluxes in a complex way to impact the convection and restratification processes in the Labrador Sea. This makes it a difficult region for ocean and
100 climate models to simulate accurately.

As more ocean model studies try to understand the Labrador Sea mixed layer, there must be evaluation with observations to make sure the models are accurately representing real world processes. Ocean simulations at eddy-permitting resolution within the North Atlantic have been plagued with a salinity
105 drift. Models tend to produce mixed layers that are too deep compared with observations in the Labrador Sea (Rattan et al., 2010), and lower resolution models tend to overestimate LSW formation compared to models run at higher resolution (Garcia-Quintana et al., 2019; Hirschi et al., 2020; Koenigk et al., 2021). The additional LSW can be due to the under-representation of the
110 lateral transport of buoyant waters from the boundary currents either through freshwater anomalies or by the warm salty subsurface Irminger Waters (Treguier et al., 2005; Rattan et al., 2010). Marzocchi et al. (2015) showed how a higher resolution model (ORCA12 vs ORCA025) improved the pathway and shape of the North Atlantic Current compared with satellite observations in the North
115 West Corner (50°N-50°W), improving the transport of heat and salt into the Labrador Sea, via eddies, in the model.

Not only is the horizontal resolution important to consider in an ocean model, but vertical resolution may also play a strong role. Stewart et al. (2017) argue that changing the vertical resolution changes the vertical structure of horizontal flows rather than just vertical motion. However, the best choice of
120 a vertical grid resolution is not clear at this point for an ocean model. Stewart et al. (2017) showed that by increasing the vertical resolution (from 50 levels to 75 levels) of a $1/10^\circ$ global ocean model the eddy kinetic energy and sea surface height on and surrounding the Antarctic continental shelf and slopes increased.
125 This improved the formation, shelf exchange and sinking of Antarctic Bottom Water. Colombo et al. (2020) found improvements for the representation of overflow waters at Denmark Strait with a combination of increasing vertical resolution as well as horizontal resolution.

Does changing both the vertical resolution and bathymetry impact the lateral buoyancy exchange in the Labrador Sea? And how does changing the
130 air-sea fluxes (atmospheric forcing) interact with or affect the lateral buoyancy exchange and consequently the MLD in the Labrador Sea? Model-diagnosed mixed layer depths may be representative of convective strength in the Labrador Sea and the formation of LSW. Therefore, convection and LSW formation will
135 be examined by investigating the response of the model-diagnosed mixed layer depths to lateral exchanges from the shelf to the interior of the Labrador Sea, air-sea heat fluxes, and changes in vertical resolution of an eddy-permitting forced ocean model.

2. Methods

This study will evaluate three simulations' model-diagnosed mixed layer
140 depth, with varying: vertical resolution, altered bathymetry, and atmospheric forcing. This section will describe the details of the ocean model including the different vertical resolutions and bathymetry, and atmospheric forcing datasets. This section will also include a description on how the mixed layer depth is
145 calculated in the model, and introduce the observations used to evaluate the

model-diagnosed mixed layer depth.

2.1. Ocean-Sea Ice Coupled Model

A coupled ocean-sea ice general circulation model is utilized in this study, within the Nucleus for European Modelling of the Ocean (NEMO) (Madec, 2008) framework. The ocean model used is Océan PARallélisé for ocean dy-
150 namics and thermodynamics and the Louvain-la-Neuve Ice Model is used for sea ice dynamics and thermodynamics (Fichefet and Morales Maqueda, 1997). The regional domain of the model covers the Arctic and Northern Hemisphere Atlantic Oceans (ANHA) and has two open boundaries, one at Bering Strait and the other at the latitude 20°S. The ANHA horizontal grid is extracted from
155 the ORCA global tripolar grid (Barnier et al., 2007) at a $1/4^\circ$ resolution with a horizontal grid spacing ranging from around 14 km to 18 km in the Labrador Sea; therefore, the model is eddy-permitting. All simulations start from January 2002 and are integrated to the end of December 2017. Initial and monthly
160 open boundary conditions (potential temperature, salinity, horizontal velocities, sea ice, and sea surface height) are derived from the Global Ocean Reanalyses and Simulations (GLORYS2V3) product (Ferry et al., 2008). At the lateral boundaries, a free slip boundary condition is used. No temperature or salinity restoring has been applied. Previous work has shown that to account for model
165 adjustment, a 2-year spin-up period is enough, given the simulations start from the reanalysis of GLORYS2v3 (Garcia-Quintana et al., 2019). The model output used in this study is therefore from 2004 to 2017. A comparison of the end of the simulations (December 2017) to the start (January 2002) as well as after the 2-year spin-up is shown for fields of salinity, potential temperature,
170 and velocity over the upper 450 m of the water column (Figure S1 and Figure S2).

River runoff (excluding Greenland) is provided by Dai et al. (2009). The GrIS freshwater flux is provided by Bamber et al. (2018); this includes tundra and ice sheet runoff, and iceberg discharge. The Bamber et al. (2018) data set
175 extends from 2002 to 2016, and 2016 is repeated for the year 2017 in this study.

Runoff is injected at the surface and vertically mixed over the top 30 metres of the water column along the coastline. In this study, runoff has a salinity of 0 and the potential temperature of the ocean grid cell that receives it. For the iceberg discharge an iceberg module is used. This module’s physical behaviour
180 is based on the original model of Bigg et al. (1997), implemented in NEMO by Marsh et al. (2015), with improvements from Gladstone et al. (2001); Martin and Adcroft (2010); Merino et al. (2016); Marson et al. (2018).

2.2. Vertical Representation

Although the number of vertical levels and their structure varies greatly
185 across the modelling community, many NEMO based studies use 45-50 levels (Treguier et al., 2005; Barnier et al., 2007; Masina et al., 2017) with other studies having used 75 vertical levels, such as the GLORYS2V3 product (Ferry et al., 2008). Previous work with the ANHA configuration used in this study had 50 vertical levels. Model experiments were able to reproduce observed Labrador
190 Sea mixed layer depths (e.g. Garcia-Quintana et al., 2019); however, there was a tendency for the model drift to lead to excessive convection. Therefore, the configuration required an atmospheric product with relatively weak buoyancy loss over the Labrador Sea (Pennelly and Myers, 2021). Our manuscript developed out of a plan to increase the vertical resolution to 75 layers, with the
195 default assumption that the use of additional vertical resolution would improve the quality of the simulation. Note that the 50 level experiments in this study are not twins of those in Garcia-Quintana et al. (2019) and Pennelly and Myers (2021). As well as the changes in vertical resolution (discussed further below), additional model improvements are included in this study: a switch to NEMO
200 v3.6, replacing the GrIS freshwater discharge with a new data set (Bamber et al., 2018), and the use of an iceberg module (Merino et al., 2016; Marson et al., 2018).

All experiments here use geopotential z-level coordinates with a partial step option (Bernard et al., 2006). In the vertical, the experiment with 50 vertical
205 levels has the layer thickness increase from 1.05 m at the surface level to 453.1 m

in the last level (at a depth of 5958.3 m) (Figure 1a). For the 75-level experiment, the layer thickness increases from 1.05 m at the surface to 204 m in the last level (at a depth of 6000 m). Therefore, the top 50 m of the water column has very minimal differences between 50 level and 75 level vertical grid. The maximum
210 vertical grid spacing around 500 m (for the shelf break) is around 87 m between levels 31 and 32 for the 50 vertical level structure and 57 m between levels 40 and 41 for the 75 vertical level structure. The maximum vertical grid spacing in the Labrador Sea (around 3000 m in depth) is 355 m between levels 43 and 44 for the 50 vertical level structure and is 183 m between levels 60 and 61 for
215 the 75 vertical level structure.

Bathymetry is taken from the existing global ORCA025 bathymetry (Barnier et al., 2006) which is based on a global relief model (ETOPO1) (Amante and Eakins, 2009) and a gridded bathymetric data set (GEBCO) (BODC, 2008) with modifications (Barnier et al., 2007). The BedMachineV3 data set (Morlighem
220 et al., 2017) has been interpolated and averaged onto the grid along the coast of Greenland for the 75-level experiments. This includes major improvements in deep bathymetric features such as troughs and canyons. BedMachineV3 also uses the updated gridded bathymetric data set of GEBCO2014. For a full evaluation and information about the upgrade between GEBCO and GEBCO2014
225 please see www.gebco.net.

The bathymetry in the 50-level model version is different in structure around Greenland to that in the 75-level model version. A comparison of the two vertical resolutions and the changes of the bathymetry in the northwest of the North Atlantic Ocean are shown in Figure 1. The 75-level bathymetry shows a
230 deepening in the interior of the Labrador Sea as well as a change in structure and steepness of the shelf off the west coast of Greenland when compared to the 50-level bathymetry. The 75-level bathymetry is deeper throughout most of the northwest corner of the Atlantic Ocean (Figure 1e). An additional comparison is shown of the 75-level resolution with the same bathymetric dataset as the 50-level resolution vs the 75-level resolution with the altered bathymetry
235 of BedMachineV3 dataset (Figure 1g and Figure 1h). The major difference

between these two are along the coast line, where the altered bathymetry of BedMachineV3 is deeper.

The lateral exchange between the shelf and the Labrador Sea interior may
240 be influenced by these changes in bathymetric structure in the Labrador Sea.
Changing the vertical resolution may impact the vertical structure of the horizontal flows, as Stewart et al. (2017) showed. Lateral exchange processes such as the production of eddies depend in part on the steepness of the bathymetry (Katsman et al., 2004) and so may also differ between 50 and 75 level versions.
245 The configuration with the updated bathymetry and higher resolution (75 levels) will be compared to the older and lower resolution set-up (50 levels), and the 75 level resolution with the original bathymetry will no longer be discussed.

2.3. Atmospheric Forcing

At the surface of the ocean, fluxes of heat, water, and momentum are computed using the Coordinated Ocean-Ice Reference Experiment (CORE) bulk
250 formulae (Large and Yeager, 2004). This study uses two atmospheric forcing data sets with a difference in the strength of the net buoyancy loss over the interior of the Labrador Sea. One data set used is the Canadian Meteorological Centre’s global deterministic prediction system (CGRF) which is a relatively high-resolution product providing atmospheric forcing fields to be used
255 for ocean-sea ice models (Smith et al., 2014). The temporal resolution is hourly, and the spatial resolution is 0.45° longitude and 0.3° latitude to generate an equal grid spacing of 33 km resolution at 49° north and south and a maximum longitudinal spacing of 50 km at the Equator.

260 The second data set that will be used to compare with CGRF is the Drakkar Forcing Set 5.2 (DFS) which provides three hourly atmospheric forcing fields at a spatial resolution of nearly 0.7° (~ 80 km at the Equator) (Dussin et al., 2016). The DFS data set was generated from ERA-interim, an atmospheric reanalysis produced by the European Centre for Medium Range Weather Forecasting.
265 Corrections have been applied to the ERA-interim surface variables such as radiation fluxes, wind speeds, decreased air temperature and humidity in the

Arctic, and liquid precipitation fields; for more details see Dussin et al. (2016) and Barnier et al. (2007). It should be noted that the CGRF data set does not prescribe snowfall, while DFS does, and snowfall must be hardcoded into the simulation as any precipitation prescribed by CGRF at or below freezing at 2 meters. DFS has been shown in a previous study (Pennelly and Myers, 2021) to drive a deeper mixed layer depth by removing the largest amount of buoyancy from the ocean in the Labrador Sea when compared to a set of five atmospheric products, including CGRF. CGRF was found to have overall less net heat loss over the interior of the Labrador Sea (46.6 W/m^2) than DFS (53.4 W/m^2) when averaged from 2002-2015 (Pennelly and Myers, 2021).

Experiments using the CGRF atmospheric forcing to drive the NEMO model with 50 vertical levels will be called C50, C75 refers to the 75 vertical level version driven by CGRF, and D75 will have the DFS atmospheric forcing at 75 vertical levels. A 50 vertical level version driven by the DFS atmospheric forcing is excluded from this manuscript as the mixed layer depth in the interior of the Labrador Sea essentially behaved the same as in C50. See Table 1 for further details of the three simulations.

2.4. Mixed Layer Depth

In the vertical, static instabilities, where lighter potential densities are below denser ones, may occur generally due to air-sea fluxes and sea ice formation. Convective processes can re-establish the static stability of the water column. However, due to the coarse vertical grid and the hydrostatic assumption, convection must be parametrized. The model restores the static stability of the water column by the enhancement of vertical diffusion (Madec, 2008). This is done by increasing the values of the vertical eddy mixing coefficients in regions where the stratification is unstable, for momentum as well as both temperature and salinity tracers. This rapidly mixes away any instabilities.

The model mixed layer depth presented in this study is estimated by Courtois et al. (2017) method, which is based on the Holte and Talley (2009) approach for Argo profiles. Two fittings are applied on the mixed layer and the layer

underneath. The possible mixed layer depth is calculated by the intersection of two linear fittings of potential temperature and salinity. This approach was created to avoid an overestimated mixed layer by using the NEMO default approach (density difference criterion of 0.01 kg/m^3), as discussed in Courtois et al. (2017). If the potential temperature based linear fitting produces a shallower mixed layer depth than compared to the default mixed layer depth, the mixed layer depth determined by potential temperature is chosen. If the mixed layer depth determined by the potential temperature is larger than the default approach, then the salinity based linear fitting is compared to the default mixed layer depth. If none of these fittings are suitable (i.e. shallower than the default mixed layer depth), then the default mixed layer depth is chosen.

The Courtois et al. (2017) algorithm was implemented online in the model, at every time step (1080 seconds). The mixed layer depth calculation is done at every time step, however, the final output of the mixed layer depth is averaged over the output file frequency, 5-day averages for C50, D75, and 1-day average for C75. Note that for this study’s questions, spatial, and temporal scale there was not a significant difference between the 5-day average output and the 1-day average output.

This study compares the model-diagnosed mixed layer depths with observations from the global database of mixed layer properties computed from Argo profiles (Holte et al., 2017). Argo is an international program that has been observing the top 2000 m of the ocean for over 20 years. Wong et al. (2020) shows that the Argo vertical resolution has increased over the 20 years. From 2000, on average there are about 50 to 80 discrete samples per 2,000-dbar profile, and then due to switching to Iridium telemetry, continuous data collected was averaged into smaller depth bins ($\sim 1\text{-dbar}$ or 2-dbar bins), giving profiles with higher vertical resolution. Therefore, at the beginning of the study period, 2004, the vertical resolution of Argo data and the model are within an acceptable range. Later on, post 2013, Argo will have a higher resolution than the model. This study will use the Argo profiles to assemble the observed mixed layer depths in the interior of the Labrador Sea and compare how the simulations

model-diagnosed mixed layer depth compares in time as well as spatially.

3. Results and Discussion

3.1. Shoaling of the Mixed Layer in the Labrador Sea

The model mixed layer depth, in conjunction with observations from Argo floats, will be evaluated in experiments C50 and C75 (Figure 2a). For details about the Argo data set, please see Holte et al. (2017). This study will focus on a small region in the interior of the Labrador Sea (white section in Figure 1), similar to Yashayaev and Loder (2017) and the model study from Garcia-Quintana et al. (2019) following the 3000 m isobath, where deep convection is observed to occur. Correlation coefficients of Argo observed mixed layer depths compared with different simulations, denoted as R values, are calculated based on the annual maximum of the mixed layer depth averaged over this region (Figure 2b) over 2004-2017 (Table 1). The variability of the mixed layer depth in C50 compares better with the Argo observations, with a correlation of 0.80 compared to C75 (correlation of 0.55).

In this study, a deep mixed layer refers to a depth at which the LSW is formed in the Labrador Sea (~ 1000 m to 2000 m depth; Lazier, 1980). During the first 5 years of the analysis period (2004 to 2009), there are only limited discrepancies between the experiments. Following the winter of 2009, when the maximum winter mixed layer depth is deep in both experiments, the winter maximum mixed layer depth in C75 is significantly shallower than that of C50 for every year through to 2017. Other than for the period of 2009-2011, when the maximum winter mixed layer depth from the Argo observations is consistently shallow, there is good correspondence between the maximum winter mixed layer depths from Argo and C50. Yashayaev and Loder (2016), show that Argo floats may underestimate the maximum mixed layer depths in the winters of 2009-2011. Yashayaev and Loder (2016), using multiple data sources, estimate maximum winter mixed layer depths multiple hundreds of metres deeper than from the Argo floats for these years. Looking at the distribution of Argo floats

in these years (winters of 2009-2011) suggests that there were only a limited number of Argo floats in the convection region, offshore of the 3500 m isobath (not shown).

360 Focusing on the period 2012-2017, when deep winter mixed layers were observed in the Labrador Sea (Yashayaev and Loder, 2017), there is a significant difference in the spatial structure of these deep winter mixed layers in C50 compared to C75 (Figure 3). Although both experiments find their deepest winter mixed layer depths around 58°N and 55°W, in C50 the 400 m and 800 m mixed
 365 layer depth contours extend north past 60°N and east as far as Cape Farewell. Even the 1200 m contour covers a broad region in the central Labrador Sea. Meanwhile, in C75 the winter mixed layer is deeper than 400 m only over a small region in the center of the Labrador Sea (Figure 3). For C50, the 2012-2017 average winter mixed layer depth exceeded 1600 m depth, whereas in C75
 370 the average mixed layer does not surpass 600 m. Therefore, while C50’s maximum winter mixed layer depth time series (Figure 2a and 2b) matches closely to observations, the area covered by deep mixed layers in C50 is too large. While the winter mixed layer depths in C75 are far too shallow, the spatial structure of where those ‘deep’ mixed layers occur is closer to observed.

375 The occurrence of convection and deep winter mixed layers depends on the stratification as well as the air-sea buoyancy fluxes. The strength of the stratification in the Labrador Sea, for both experiments (Figure 4a and Figure 4b), was quantified by determining the water column stability to a depth (h) and quantifying the vertical integral buoyancy anomaly to be removed (m^2/s^2) needed
 380 to overcome that stratification and mix to that depth (h). This measure is called convection resistance, or vertical integral buoyancy anomaly to be removed, where high convective resistance indicates the presence of a “barrier to convection” as Bailey et al. (2005) discussed. Convection resistance (CR) is defined in Equation 1, based on previous work by Holdsworth and Myers (2015),
 385 with concepts of buoyancy anomalies as described in Bailey et al. (2005), and

Frajka-Williams et al. (2014):

$$CR(h) = \frac{g}{A\rho_0} \int \int_A \left[h\sigma_\theta(h) - \int_0^h \sigma_\theta(z)dz \right] dA \quad (1)$$

where g is the acceleration due to gravity (9.81m/s^2), A is the area of each grid cell, and ρ_0 is the reference density (1026 kg/m^3 ; Madec, 2008). The amount of integral buoyancy in a well-mixed column of fluid with a potential density
390 of $\sigma_\theta(h)$ is compared to that in the modelled water column with a potential density of $\sigma_\theta(z)$ at each depth ($z < h$). $h = 2000\text{ m}$ is chosen in Equation 1 which gives the total amount of vertical integral buoyancy anomaly to be removed to mix the water column to a depth $h = 2000\text{ m}$ (which is considered to be the maximum depth of the mixed layer in this study; those areas with
395 water depths less than 2000 m are ignored for this analysis). $CR(h)=0$ implies a well-mixed fluid, $CR(h)>0$ implies a stable density stratification, and $CR(h)<0$ implies an unstable density stratification.

There is significantly greater convection resistance throughout the Labrador Sea in C75 (Figure 4b) than C50 (Figure 4a). In both experiments, the lowest
400 convection resistance is in the western Labrador Sea, consistent with where the mixed layers are deepest. In C75, the western Labrador Sea is the only portion of the basin with convection resistance less than $0.6\text{ m}^2/\text{s}^2$, with the convection resistance increasing from there, almost uniformly, in all directions. In C50, convection resistance remains low over a much larger area, consistent
405 with the 400 m winter mixed layer depth contour. The difference plot of C50-C75 (Figure 4c) shows a big increase in convection resistance, exceeding $0.7\text{ m}^2/\text{s}^2$, in the north and south of the Labrador Sea, with smaller differences in between, approaching $0\text{ m}^2/\text{s}^2$, reaching offshore from the West Greenland Current.

410 The large differences in convection resistance between C50 and C75 suggest that there must be significant differences in the water mass properties in the interior of the Labrador Sea between the two experiments. Given the significant differences in winter mixed layer depth, a profile of potential temperature and

salinity for the Labrador Sea interior for 2012 to 2017, showing the wintertime
 415 profile in C50 and C75, is examined (Figure 5). Comparing the 50th percentile
 in the top 200 m, the interior of the Labraor Sea in C75 is cooler by $\sim 2^\circ\text{C}$ and
 fresher by 0.3 than in the profile for C50. In the top 100 m of the experiments
 the density of the 50th percentile curve is within the range of $27.4 - 27.7 \text{ kg/m}^3$
 for C75 and $27.6 - 27.8 \text{ kg/m}^3$ for C50. The profile in C75 is more stratified,
 420 with a lighter water mass than in C50; therefore, C50 has a winter-water column
 that is more mixed.

From 2012 to 2017, the upper 450 m in the Labrador Sea is on average
 significantly saltier (Figure 6a) and warmer (Figure 6b) in C50 than C75. An
 averaging depth of 450 m is considered here because it includes both the upper
 425 ocean freshwater layer as well as the main core of the Irminger Water.

Another way to examine the property changes is to compute the freshwater
 and heat content for the interior of the Labrador Sea (Figure 7; Equation 2
 and Equation 3). The freshwater content (FWC; units in m^3) relative to a
 reference salinity $S_{ref} = 34.97$, which is the top 1500 m model Labrador Sea
 interior-averaged salinity.

$$FWC = \int \frac{S_{ref} - S}{S_{ref}} dV \quad (2)$$

where S is model salinity. The heat content (HC; in TW) is defined as:

$$HC = \rho_0 C_p 10^{-12} \int (T - T_{ref}) dV \quad (3)$$

where T is the model potential temperature, $T_{ref} = 4^\circ\text{C}$ is the reference
 temperature, which is the top 1500 m model Labrador Sea interior-averaged
 temperature. ρ_0 is the reference density (1026 kg/m^3 ; Madec, 2008) and C_p is
 430 the specific heat capacity of sea water ($3992 \text{ J/kg/}^\circ\text{C}$; IOC, SCOR, and IAPSO,
 2010). See Figure S3 where $T_{ref} = -2^\circ\text{C}$, and $S_{ref} = 34.8$ (Aagaard and
 Carmack, 1989).

From 2004 to 2009, there was little difference in the freshwater content be-
 tween the experiments with it slowly decreasing with time in all runs, consistent

435 with model drift (Rattan et al., 2010). However, after 2009 the freshwater content of the runs diverges suddenly and significantly, increasing in C75 while it continues to slowly decline in C50 (Figure 7). The heat content begins to diverge earlier, in 2006, with the upper ocean in C50 significantly warmer over time than in C75. The opposing behaviour in freshwater and heat content in
 440 the interior for C50/C75 (saltier and warmer in C50 and fresher and colder in C75) may have resulted in little net effect on density. However, there would be a greater likelihood of deep mixing if the saltier ocean in C50 could be cooled sufficiently in winter, which is what occurred in that experiment.

3.2. Lateral Buoyancy Fluxes Impact on the Depth of the Labrador Sea Mixed 445 Layer

The exchange between boundary and interior of the Labrador Sea will be examined to explain the differences, previously discussed, in potential temperature and salinity (Figure 5 and Figure 6) as well as heat and freshwater content (Figure 7).

450 Similarly as with Equation 2 and Equation 3, the freshwater flux (FW_{flux}) and temperature flux (T_{flux} ; units in TW) are defined as:

$$FW_{flux}(t) = \int_0^L \int_0^{H(x)} \frac{S_{ref} - S}{S_{ref}} U(t, z, x) dz dx \quad (4)$$

$$T_{flux}(t) = \rho_0 C_p \int_0^L \int_0^{H(x)} (T(t, z, x) - T_{ref}) U(t, z, x) dz dx \quad (5)$$

where $S_{ref} = 34.97$ and $T_{ref} = 4^\circ \text{C}$, which is the top 1500 m model Labrador Sea interior-averaged salinity and temperature. L is the length along the section, $H(x)$ is the water depth along the section, and U is the velocity perpendicular
 455 to the section. See Figure S4 where $T_{ref} = -0^\circ \text{C}$, and $S_{ref} = 34.8$ (Aagaard and Carmack, 1989). Throughout the discussion of the results, when there is a lack of freshwater or when the freshwater transport is negative (freshwater export) this can imply an increase in salinity. Therefore, the freshwater export will highlight the importance of changes in salinity and its role in impacting the
 460 Labrador Sea’s mixed layer.

The spatial and temporal variability of the exchange between the interior and surrounding regions is shown in Figure 8, across the white section in Figure 1. This figure shows the summation of the fluxes over 0 to 1500 m of the water column. Exchanges from the west (1000-1400 km) and north (0-200 km) are generally small and similar between the two experiments (C50 and C75). Exchange from the West Greenland Current (200-700 km) and the south (700-1000 km) explain the larger heat and salt content in the interior of the Labrador Sea in C50, as there was continual transport of warm and salty waters into the basin interior (freshwater transport out of the basin). In C75, these exchanges are much smaller, especially from the West Greenland Current (volume flux \sim 1 Sv, compared to volume flux of 2 Sv in C50).

Without this source of heat and salt, the interior of the Labrador Sea in C75 freshens (Figure 7a) and cools (Figure 7b). Exchange of warm water across the southern boundary of the Labrador Sea interior region, in C75, increases around 2012 (20 TW; Figure 8h) potentially explaining the stabilization of the freshwater and heat content time series after that date (Figure 7). Export to the south, from the interior of the Labrador Sea, in C75 is about half of the export in C50 for freshwater transport (-2 mSv vs -4 mSv; Figure 8e and Figure 8d, respectively). From 2014 to 2016, C75 has a strong exchange of freshwater transport into and out of the basin around 800 km to 1000 km. Import from the south (around 700-1000 km), to the interior of the Labrador Sea, in C75 is also about half of the import in C50 for heat transport (\sim 2 TW vs 4 TW; Figure 8h and Figure 8g, respectively). Therefore; the south portion of the basin is an important region for exchanges in the freshwater flux (potentially from LSW export or changes in the North Atlantic Current).

The modified Irminger Water transported into the Labrador Sea around Cape Farewell (location shown in Figure 1) is an important source of heat and salt for the West Greenland Current. A time series of the westward flux of Irminger Water (defined by $S > 34.8$ and $\rho < 27.68 \text{ kg/m}^3$) past Cape Farewell is shown in Figure 9. Following 2009, the volume flux is larger in C50 than C75 (\sim 12 Sv vs \sim 6 Sv; Figure 9a). On average, C50 has a stronger eastward

freshwater export (- 62 mSv), about three times larger than in C75 (- 21 mSv; Figure 9b, Table 1), implying an increase in salinity. Additionally, C50 has on average a greater temperature flux westward (210 TW), about two times larger
495 than in C75 (97 TW; Figure 9c; Table 1). But it is not just that more heat and salt are entering the Labrador Sea in C50 than in C75, the fluxes are much more variable and the strength of the transient kinetic energy (TKE) also differs.

The average TKE (2012 to 2017) of the top 500 m of the water column, in C50 and C75, is shown in Figures 10a and 10b. The monthly TKE was
500 calculated using Equation 6; u^2 and v^2 were calculated for every five-day model zonal and meridional velocities and then averaged over the month, and \bar{u} and \bar{v} denote the monthly mean average velocities.

$$TKE = \frac{(\bar{u}^2 - \bar{u}^2) + (\bar{v}^2 - \bar{v}^2)}{2} \quad (6)$$

The differences between the two simulations are shown in Figure 10c, where the TKE in C50 has the TKE in C75 subtracted from it. Therefore, positive
505 (negative) values indicate that C50 (C75) has higher TKE values. The TKE in C50 is larger by $\sim 20 \text{ cm}^2/\text{s}^2$ offshore of the WGC near the 3000 m isobaths, and by $\sim 15 \text{ cm}^2/\text{s}^2$ in the northwest corner along the 2000 m isobath. The TKE in C75 is larger by $\sim 10 \text{ cm}^2/\text{s}^2$ along the 2000 m isobath off the south portion of the Canadian shelf. The decrease in the TKE in the 75-level experiment
510 may arise from the 50-level experiment's vertical structure having a coarser resolution and a steeper gradient in this region (Figure 1a) which may promote more instabilities and therefore mixing.

The “steeper gradient” referred to here is the coarser model grid’s “step-like” feature along the slope (shelf). The model simulates the bathymetry in steps,
515 like a staircase. With a higher vertical resolution (C75) there would be more steps on the staircase, and with a lower vertical resolution (C50) there would be fewer steps on the staircase. There would be a bigger jump from one step to the next, in comparison; therefore, the slope (shelf) would have a steeper (in fact, vertical) gradient. Whereas in C75, although this has deeper bathymetry

520 in some areas, the slope is better resolved with less extensive regions of vertical
 wall. Additionally, C50 has deeper depths than C75 south of Cape Farewell
 along the continental slope (Figure 1e), which may also promote more transport
 of warm salty waters as seen in Figure 9. Given the horizontal resolution of $1/4^\circ$,
 it is not surprising that the TKE in these simulations is significantly less than
 525 in observations (Fratantoni, 2001); this is a known issue with models that are
 not eddy-resolving (Chanut et al., 2008; Pennelly et al., 2019).

The strong transport of warm and salty water into the southern part of the
 Labrador Sea interior in C50 is through the Cape Farewell section (Table 1),
 consistent with the expanded band of low convection resistance stretching south
 530 of Cape Farewell (Figure 4a). Without it, as shown in C75, convection resistance
 remains large in this southern region (Figure 4b). A large transport of Irminger
 Water north in the West Greenland Current, in C50, leads to saltier conditions
 in the northern Labrador Sea (Figure 6). Therefore, low convection resistance
 (Figure 4a) and a broad northward extension of the region of deep winter mixed
 535 layers occurs (Figure 3a). Although the maximum winter mixed layer depths in
 C75 are shallower than observed, the spatial extent of deep winter mixed layers
 is more realistic in C75 than in C50 (Figures 3b and 3d).

3.3. *Influence of Atmospheric Buoyancy Fluxes on the Depth of the Labrador Sea's Mixed Layer*

540 The mixed layer in the Labrador Sea is a balance between atmospheric buoy-
 ancy loss and lateral buoyancy exchange from the boundary currents. Section
 3.2 showed how differences in the lateral exchange between the 50 and 75 level
 model versions impact the water properties in the interior of the Labrador Sea.
 In this section, two experiments with different air-sea buoyancy forcing will also
 545 be compared.

Pennelly and Myers (2021) used a 50 vertical level configuration similar
 to C50 and forced with the same CGRF forcing (Smith et al., 2014) as that
 employed here; this has been shown to have weaker surface buoyancy loss over
 the Labrador Sea than other atmospheric forcing products used in their study.

550 In the 75 vertical level version (C75, which also has different bathymetry along
the Greenland shelf), the water mass properties in the interior of the Labrador
Sea are different and the CGRF atmospheric forcing does not result in strong
enough buoyancy loss to produce deep mixed layers. Therefore, an equivalent 75
level experiment forced with DFS (Dussin et al., 2016), one of the atmospheric
555 products identified by Pennelly and Myers (2021) to have strong buoyancy loss
over the Labrador Sea (this study refers to this model simulation as D75), is
carried out.

The monthly average buoyancy flux, B_φ ($\text{N}/\text{m}^2\text{s}$), into the ocean over the in-
terior of the Labrador Sea can be computed using an equation from Sathiyamoor-
560 thy and Moore (2002) and Gill (1982) that sums the thermal and haline forcing
contributions:

$$B_\varphi = b_q + b_s$$

with (7)

$$b_q = \frac{g\alpha}{C_p}\varphi_q \text{ and } b_s = gS\beta\varphi_s$$

For the buoyancy heat flux (b_q), g is gravity, $\alpha = \rho^{-1}\partial\rho/\partial T$ is the thermal
expansion coefficient of seawater at the surface, C_p is the specific heat capacity
of water (3992 J/kg/ $^\circ\text{C}$; IOC, SCOR, and IAPSO, 2010), and φ_q is the heat
565 flux into the ocean at the surface. For the buoyancy salt flux (b_s), S is the
salinity at the surface, $\beta = \rho^{-1}\partial\rho/\partial S$ is the haline contraction coefficient and
 $\varphi_s = (P - E)$ is the ocean salt flux at the surface where P is the precipitation
and E is the evaporation. The haline contribution comes from the addition or
removal of freshwater. The surface of the ocean gains buoyancy when $B_\varphi > 0$
570 and thus becomes less dense, while the surface is losing buoyancy and becoming
denser when $B_\varphi < 0$.

The time series of the buoyancy forcing over the interior of the Labrador
Sea is shown in Figure 12. All three experiments show similar seasonality for
the surface buoyancy loss and gain over the Labrador Sea. In C75, the ocean
575 surface of the Labrador Sea gains more buoyancy throughout the years than

in C50. In C50 the ocean surface gains the least amount of buoyancy and additionally loses similar amounts of buoyancy to the atmosphere as in C75. Therefore, there is stronger net buoyancy loss observed in C50 than in C75. It may seem strange that these two experiments, which use the same atmospheric forcing, have a different wintertime buoyancy loss (see Figure 12a, 2011 to 2017). However, the ocean surface heat fluxes are computed from bulk formulae (Large and Yeager, 2004) and both the latent and sensible heat components, as well as the evaporation flux (the saline buoyancy flux), depend on the sea surface temperature. Given the warmer upper ocean in C50 (Figure 6b, 7b), cold surface air temperatures in winter lead to greater cooling, heat fluxes, and buoyancy loss despite a stronger saline buoyancy gain through enhanced evaporation. Given the stronger buoyancy loss and weak stratification (Figure 4a), widespread and deep winter mixed layers develop across the Labrador Sea in C50. Meanwhile, with cooler pre-winter sea surface temperatures leading to weaker buoyancy loss in C75, the result is that the larger convection resistance in this experiment (Figure 4b) cannot be overcome and only shallow and limited convection occurs. The surface layer of the Labrador Sea in D75 has a different net annual air-sea buoyancy flux, and gains and loses less buoyancy than in C75 (Figure 12).

Mixed layer depths in the Labrador Sea are deeper in D75 than C75, with the winter maxima close to C50 (Figure 2). The variability in maximum winter mixed layer depth in D75 is now closer to the Argo observations with a correlation of 0.77 (Table 1). The spatial structure of the mixed layer shows a broader and deeper structure in D75 than C75 (Figure 3). D75 shows a mixed layer depth of 400 m closer to the Irminger Sea which is more in-line with observations (Yashayaev and Loder, 2017) than the other simulations in this study, as C50 overestimates the depth while C75 underestimates it (Figure 3f). Compared to C50, the extent of excessively deep mixed layers north of 60°N is reduced (Figure 3). The overall structure of the observed mixed layer depths from Argo matches best with mixed layer depth in D75 (Figure 3f). The convection resistance in the interior of the Labrador Sea is $0.2 \text{ m}^2/\text{s}^2$ less in D75 than in C75, and there is even more of a difference in convection resistance north

($0.5 \text{ m}^2/\text{s}^2$) and south ($\sim 0.6 \text{ m}^2/\text{s}^2$) of the Labrador Sea core convection region compared to C75 (Figure 4e). In the Labrador Sea, a stronger buoyancy loss in D75 created a weaker stratification than in the too strongly stratified C75.

610 In D75, the deformation radius (Figure 11c) is less than the model grid size in the interior of the Labrador Sea; however, both C75 and D75 better resolve the deformation radius off the west coast of Greenland than compared to the C50 (less vertical resolution and change in bathymetry).

On average in the winter, the top 1500 m of the Labrador Sea’s interior

615 in D75 had saltier water than in C75 (Figure 5). In D75, there was less cold, fresh, and light water ($T < 3^\circ\text{C}$, $S < 34.8$) than in C75. Therefore, more of the light upper water mass has been transformed into denser water in D75. The Labrador Sea has a warmer boundary current ($+0.04^\circ\text{C}$) in D75 than in C75, but, due to stronger buoyancy losses, has a saltier and cooler interior

620 ($\Delta S \approx 0.01$, $\Delta T = -0.04^\circ\text{C}$; Figure 6), aiding the strengthening of winter convection. The freshwater content in the interior of the Labrador Sea in D75 does not increase as much as in C75 following 2009 (Figure 7a). Strong heat loss still occurs in the winter (Figure 7b) due to the larger air-sea buoyancy forcing, even though D75’s Labrador Sea interior gained more heat content than C75

625 throughout the period (Figure 7).

The differences in freshwater and temperature fluxes into the interior of the Labrador Sea between C75 and D75 are not large when compared to the differences between C75 and C50 (Figure 8). The largest differences between D75 and C75 occur in the south of the Labrador Sea, where the North Atlantic

630 Current exchanges warm salty waters with the interior (around km marker 700-900). In C75, the temperature flux is stronger (around 900 km marker) from 2004-2008, 2011-2014 compared to D75’s temperature flux; however, the interior Labrador Sea heat content was higher in D75 (Figure 7b). For freshwater flux into the interior (Figure 8e. and 8f. for C75 and D75), the Hovmöller plots

635 show a similar structure between the two experiments, except for two periods. In 2004 to 2005 around km marker 900 to 1200 and in 2013 to 2017 around km marker 800 to 1000. Therefore, since there are more differences between C50

and C75, it would show that the behaviour of the salt and heat import may be more closely linked to the change in number of vertical levels or representation
640 of the topography, rather than due to a difference in atmospheric forcing fields.

There was less volume transport of Irminger Water westward at Cape Farewell in D75 (3.0 Sv) than in C75 (4.5 Sv) on average (Figure 9a; Table 1). For the Cape Farewell section in D75 there was also slightly less salt and temperature flux westward than in C75 (Figure 9b and Figure 9c). Myers et al. (2007) esti-
645 mated around 4.9 ± 1.1 Sv, 98 ± 22 TW, and 10.9 ± 2.2 mSv for the volume, heat, and salt fluxes, respectively, over 1995-2005 from observations. Although in this study the averaging period is different (2004-2017), and there is significant temporal variability in Irminger Water exchange at Cape Farewell, an examination of the relative values help understand the model's lateral exchange.

650 The large fluxes (Table 1), especially for freshwater, in C50 suggest that this is a large location for freshwater export (increasing the salinity) and source of much of the warm water that reaches the Labrador Sea interior, reduces stratification, and promotes broad and deep mixed layers. Given the experiments were forced with the same atmospheric dataset in C75 as C50, the reduced input of Irminger
655 Water at Cape Farewell in C75 must be related to formation or pathway changes in the eastern Subpolar Gyre basin brought about by the change in details of the bathymetry (not explored here). D75 has the freshwater flux closest to the observed (remembering the different time periods), although weaker volume and temperature fluxes. However, this increased freshwater flux appears to be suf-
660 ficient, in combination with strong atmospheric forcing, to allow for significant and deep mixed layers in the Labrador Sea.

Figure 13, shows the net lateral buoyancy flux of the interior of the Labrador Sea inferred from Equation 7 while integrating over the surface area of the lateral boundaries of the convection region. It is not surprising that C75 and D75 have
665 similar net lateral buoyancy fluxes as fluxes shown in Figure 8 were similar as well as the transport from Cape Farewell (Figure 9). C50 gains more buoyancy at certain times (Figure 13), due to the import of warm waters (as seen in Figure 8 and Figure 9).

The magnitude of TKE in the West Greenland Current and along the Labrador
670 Shelf is smaller in D75 compared to C75 ($20 \text{ cm}^2/\text{s}^2$ less; Figure 10e). In D75,
the TKE is lower where the boundary currents along the Labrador Sea are
warmer than in C75 (Figure 6c). The changes in TKE between C75 and D75
indicate that the changes in water mass properties are having a significant ef-
fect on the ocean currents' kinetic energy (velocities). Additionally, given the
675 stronger boundary current transport at Cape Farewell in C75 than D75, there
is an increased likelihood of baroclinic instability.

4. Conclusion

The role of ocean-atmosphere buoyancy fluxes and lateral buoyancy exchange
on the mixed layer depths in the Labrador Sea and its representation in an eddy-
680 permitting ocean model have been investigated. The analysis focused on the
model-diagnosed mixed layer depths as a representation of convection and LSW
formation in the real world. This study found, as in Stewart et al. (2017), that
changing vertical resolution changes the horizontal flows; specifically, in a config-
uration with 75 levels and modified bathymetry along the Greenland shelf (C75)
685 compared with a 50-level configuration (C50). The lateral exchange of buoyancy
between the shelf and to the interior was impacted by the change in the details
of the bathymetry resulting from the 75-level model's better representation of
the Greenland shelf. At higher vertical resolution, the boundary current was
more constrained to follow the slope; therefore, the lateral exchanges of heat
690 and salt between the shelf and the interior were smaller. There is an increased
freshwater (reduction of salinity) import into the Labrador Sea via the Irminger
and North Atlantic Currents in the 75-level model compared with the 50-level
model, allowing the Labrador Sea to become more buoyant. At Cape Farewell,
there is lower TKE in C75 compared with C50. In C75, the westward fluxes of
695 heat and salt associated with Irminger Water at Cape Farewell are 50 % and 33
% of their values in C50, respectively. Therefore, the exchange of Irminger Wa-
ter into the interior of the Labrador Sea is primarily responsible for the changes

in salt content in the interior of the Labrador Sea.

Without this source of salt and heat the Labrador Sea is able to freshen
700 and cool. And with a weaker surface buoyancy loss, the mixed layer depth
was shallow (deep convection does not occur). This prevents a salinity drift in
the model's Labrador Sea which has plagued the 50-level model and resulted
in overly deep mixed layers, a common problem in other model simulations too
(Rattan et al., 2010; Garcia-Quintana et al., 2019). The different lateral ex-
705 change in the 75-level model leads to a stronger stratification in the interior of
the Labrador Sea with stronger convection resistance which creates an unreal-
istically shallow mixed layer. With cooler pre-winter sea surface temperatures
leading to a weaker buoyancy loss in the interior of the Labrador Sea for C75,
the result was that the greater convection resistance in this experiment cannot
710 be overcome and only shallow and limited convection occurs.

Argo observations show that deep wintertime mixed layer occurred through-
out the study period (Figure 2a). Therefore, the extreme shallowing of the
mixed layer in later years in C75 is not realistic. Applying a strong buoyancy
loss over the Labrador Sea in the 75-level model with atmospheric forcing from
715 DFS (Dussin et al., 2016) increases the buoyancy loss from the surface of the
ocean to the atmosphere (D75). The Labrador Sea in D75 is therefore able to
generate a deeper winter mixed layer than in C75, with convection resistance
decreasing, weaker stratification, and stronger buoyancy loss at the surface.
Less freshwater content and stronger buoyancy loss create a saltier and cooler,
720 therefore denser, ocean surface in the Labrador Sea interior, compensating for
the change in lateral advection. This enables a break-through of the buoyant
cap and strengthened winter convection, which generated a realistic deep mixed
layer with depths closer to observed values.

This manuscript has highlighted that the configurations showed changes in
725 the lateral and air-sea heat fluxes arise due to changes in surface forcing, vertical
resolution, and bathymetry. This has a significant impact on the stratification
and the deep water formation in the Labrador Sea in the configurations. This
study has tested multiple configurations and identified a way to reduce model

salinity drift. The lateral advection of salt was impacted most by changes in
730 bathymetry and in the number of vertical levels, rather than by changes in
atmospheric forcing. An increase in vertical levels decreased the salt import
into the Labrador Sea. Further investigation is needed to assess the importance
in the changes of the North Atlantic Current, and larger scale ocean currents.
Therefore, longer-term climate studies need to be careful with the choice of
735 ocean model vertical resolution and bathymetry. The bathymetry along the
Greenland shelf, and the lateral exchange with the boundary current may play
a critical role in the downstream, larger-scale ocean circulation. This could be
especially important for longer-term climate studies.

Competing Interests

740 The authors declare that they have no conflict of interest.

Author Contributions

L.C.G. was responsible for the analysis and ran all of the model experiments.
C.P. provided insight, manuscript edits, and performed some of the calculations:
the heat flux at Cape Farewell, convective resistance, and buoyancy flux between
745 the atmosphere and ocean surface. H.L.J. and P.G.M. provided advice, insight,
and manuscript edits.

Acknowledgements

We would like to give thanks to the NEMO development team and the
Drakkar project for providing the model and technical support, and to West-
750 grid and Compute Canada for computational resources, where all model exper-
iments were performed and archived (<http://www.computeCanada.ca>). We are
gratefully for the financial and logistic support of the grants from the Natural
Sciences and Engineering Research Council (NSERC) of Canada. These include
Discovery Grant (rgpin227438) awarded to Dr. P.G. Myers, Climate Change and

755 Atmospheric Research Grant (VITALS - RGPCC 433898), International Create
(ArcTrain - 432295) and support from NSERC project no RGPIN-2018-05009.
This work is a contribution to ArcticNet, a Network of Centres of Excellence
Canada.

Financial Support

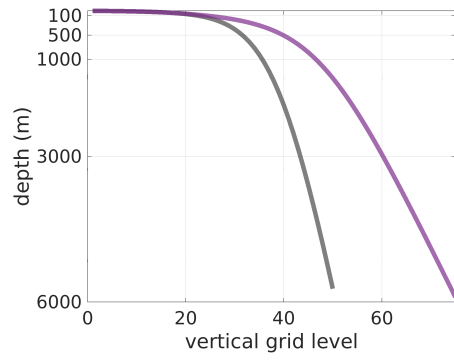
760 This research has been supported by the Natural Sciences and Engineering
Research Council of Canada (grant nos.rgpin227438, rgpcc433898, 432295, and
nos.rgpin-2018-05009).

Data Availability

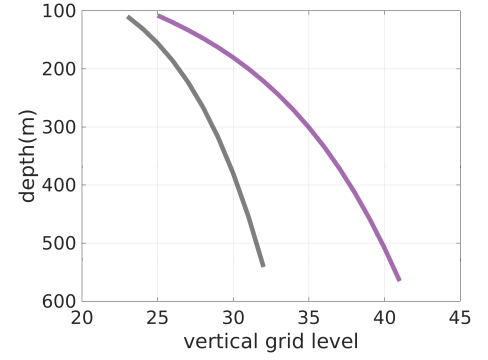
The Argo data used were collected and made freely available by the In-
765 ternational Argo Program and the national programs that contribute to it.
(<https://argo.ucsd.edu>, <https://www.ocean-ops.org>). The Argo Program is part
of the Global Ocean Observing System (<http://doi.org/10.17882/42182>).

Table 1: Simulations used in this study vary in the number of vertical levels (VL) (50 levels vs. 75 levels) and atmospheric forcing (the Canadian Meteorological Centre’s global deterministic prediction system (CGRF) (Smith et al., 2014) vs. the Drakkar Forcing Set 5.2 (DFS) (Dussin et al., 2016)). Correlation coefficients of Argo observed mixed layer depth compared with the different simulations from 2004 to 2017 for the Labrador Sea interior (Figure 1) are shown in the 4th column. Columns 5 through 7 show the average (2004 to 2017) fluxes of volume (V), temperature (T), and freshwater (FW) (seen in Figure 9) through the Cape Farewell section (shown in Figure 1), where positive numbers mean westward and negative numbers mean eastward (for the freshwater (FW) flux, negative values mean a freshwater export, implying an increase in salinity.)

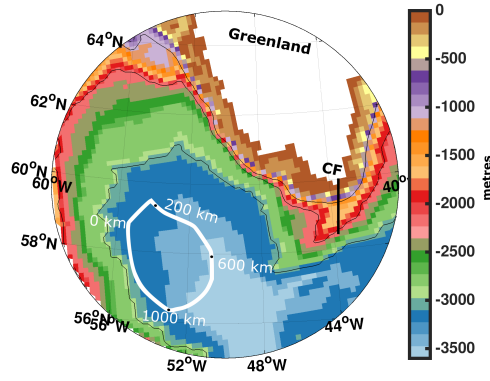
Simulation	VL Resolution	Atmospheric Forcing	Correlation with Argo	V Flux (Sv)	T Flux (TW)	FW Flux (mSv)
C50	50	CGRF	0.80	8.40	210 .23	- 61.63
C75	75	CGRF	0.55	4.45	96.67	- 21.24
D75	75	DFS	0.77	3.03	65.40	- 14.03



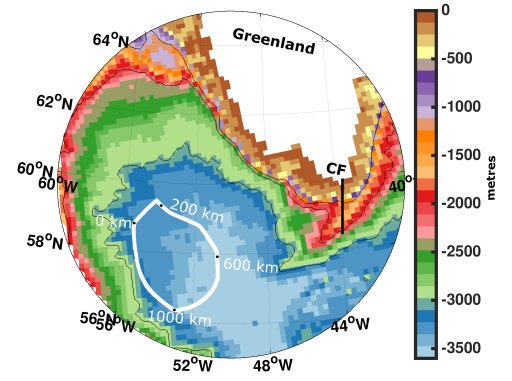
a.



b.



c.



d.

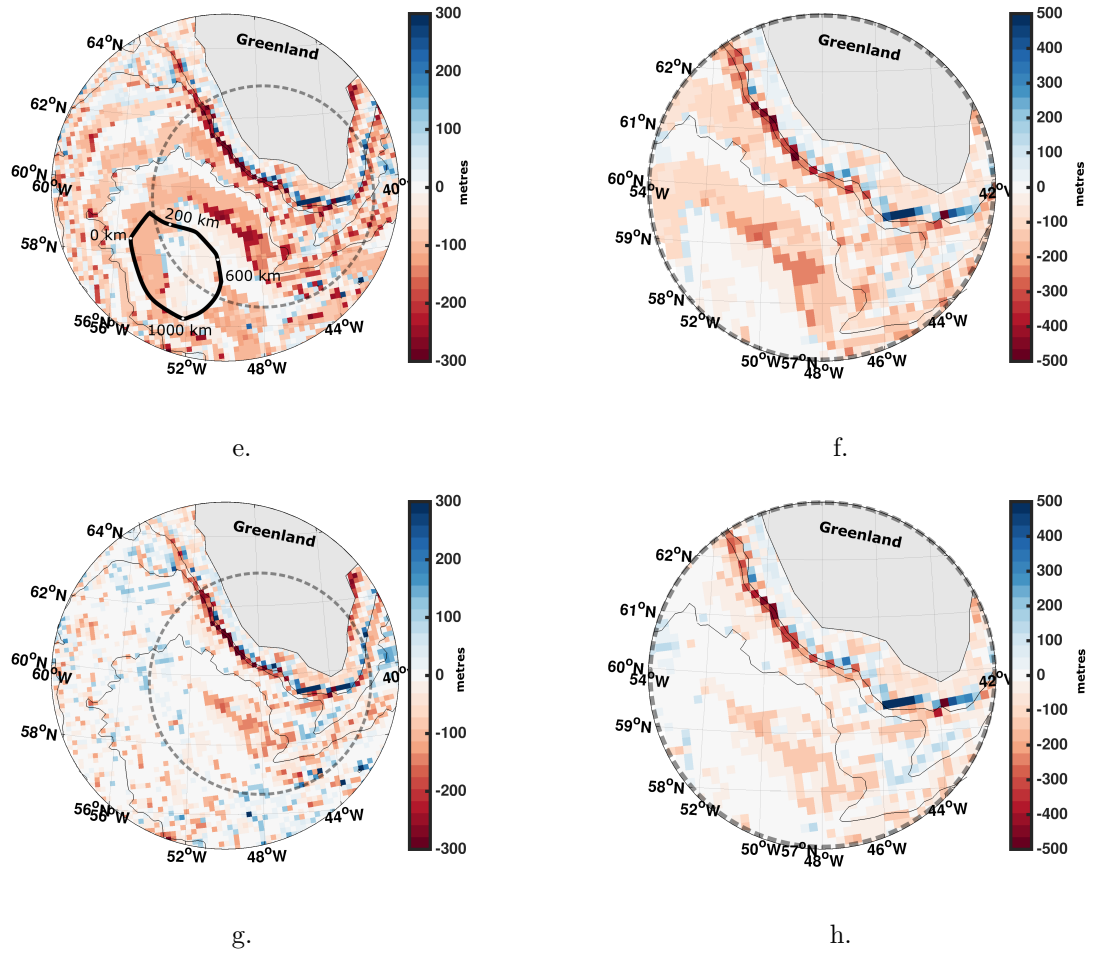
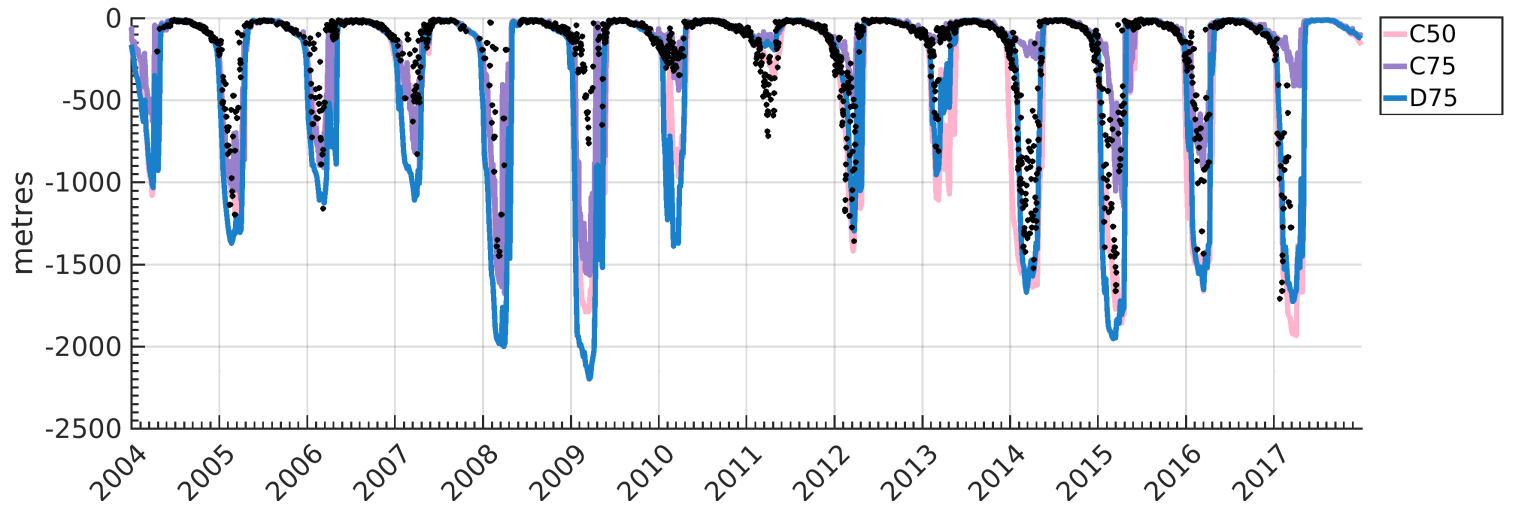
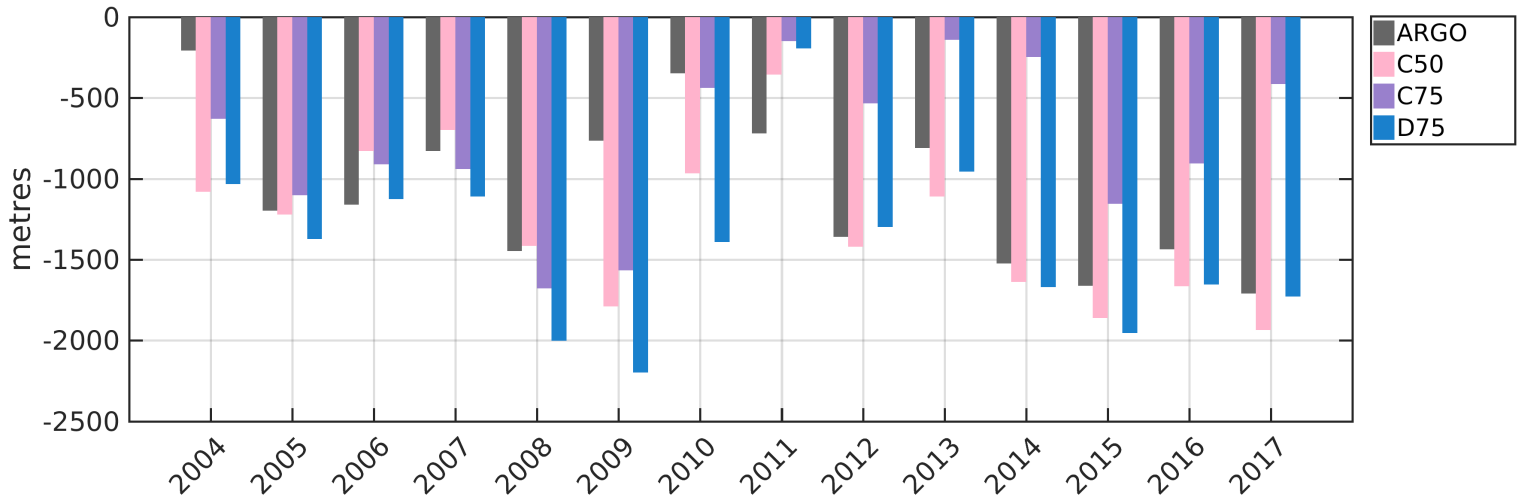


Figure 1: Panel a) shows the comparison of the vertical resolution at 50 levels (grey) and 75 levels (purple). Panel b) is a zoom-in of the y-axis in (a) at intermediate depths (~ 100 m to ~ 600 m). Panels c) and d) show the model bathymetry for 50 levels (c) and 75 levels (d). The colour denotes depth in metres. The area of the interior Labrador Sea is shown in the white section. Numbers along the white line indicate kilometre markings along the section. This section was selected following Yashayaev and Loder (2017) and the model study from Garcia-Quintana et al. (2019) following the 3000 m isobath. The Cape Farewell section is indicated by the black line labelled CF. Panel e) shows the difference in bathymetry between the 50 level and the 75 level configuration, where negative numbers show where the 75 level configuration is deeper. Panel f) is a zoom-in of the dashed circle in (e) on the West Greenland Shelf. Panel g) shows the difference in bathymetry between the 75 level resolution with the same bathymetry as the 50 level vs the 75 level resolution with the altered bathymetry (used in C75), where negative numbers show where the latter is deeper. Black lines show isobaths of 1000 m, 2000 m and 3000 m using the bathymetry from C50 for panel (c), C75 for panel (d), panel (e), and C75.

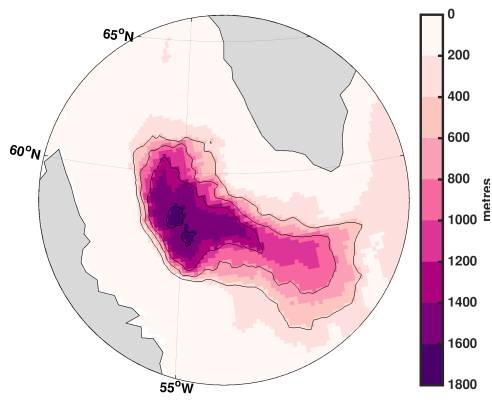


a.

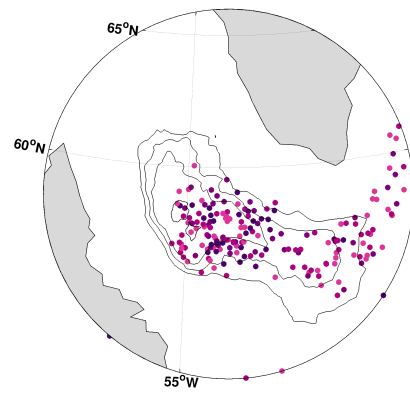


b.

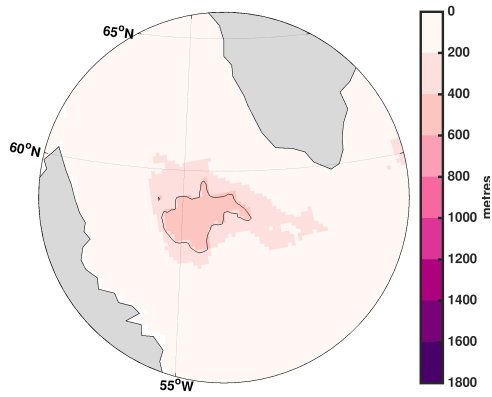
Figure 2: (a) Mixed layer depth averaged over the interior of the Labrador Sea (white section in Figure 1). Each experiment's five-day averaged model output of mixed layer depths is averaged spatially over the interior of the Labrador Sea. Argo observations are also averaged over the interior for each day (black circles). (b) Maximum mixed layer depth over each year.



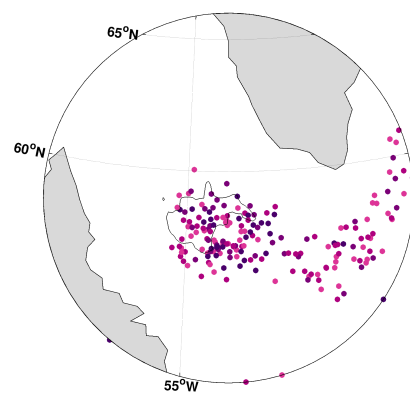
a. C50



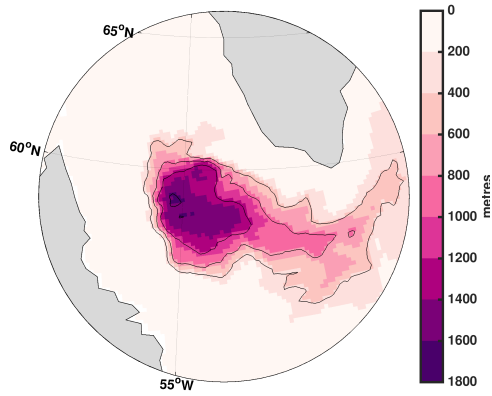
b. Argo



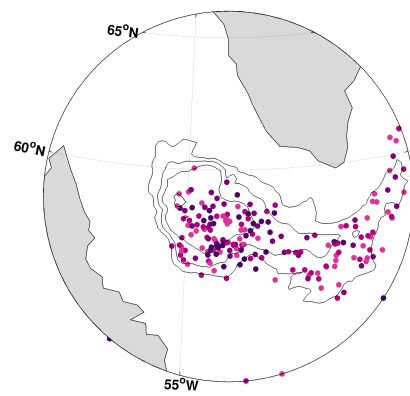
c. C75



d. Argo

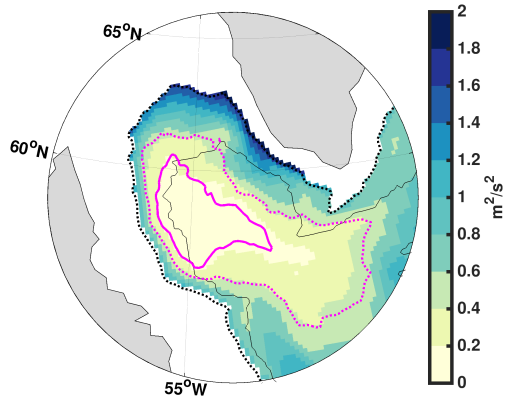


e. D75

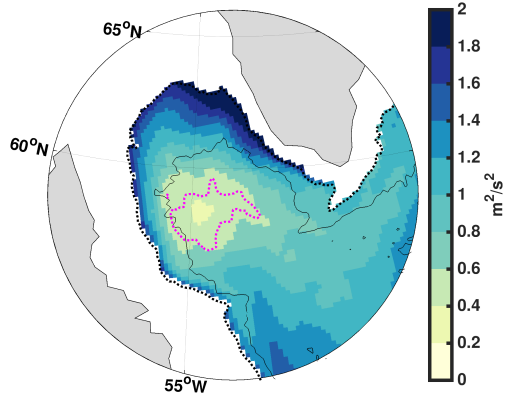


f. Argo

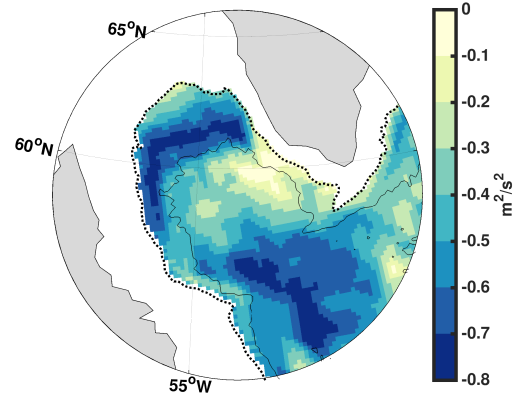
Figure 3: Mixed layer depths averaged for January, February and March of years 2012 to 2017. Post 2010 years chosen based on known timing of deep mixed layer depths from observations (Argo floats) and where configurations deviate from each other. Left column shows a different experiment, and the right column shows the observed depth from Argo floats with corresponding experiment's depth contours in each row: a) C50, b) Argo and C50, c) C75, d) Argo and C75, e) D75, and f) Argo and D75. Contour lines show intervals of 400 m (400 m, 800 m, 1200 m and 1600 m).



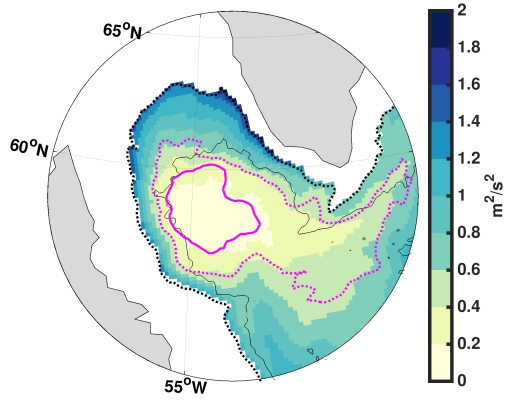
a. C50



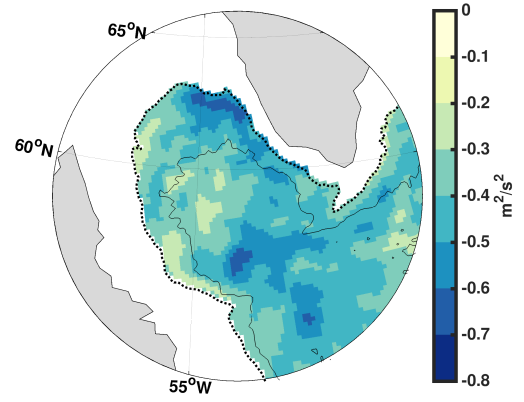
b. C75



c. C50-C75

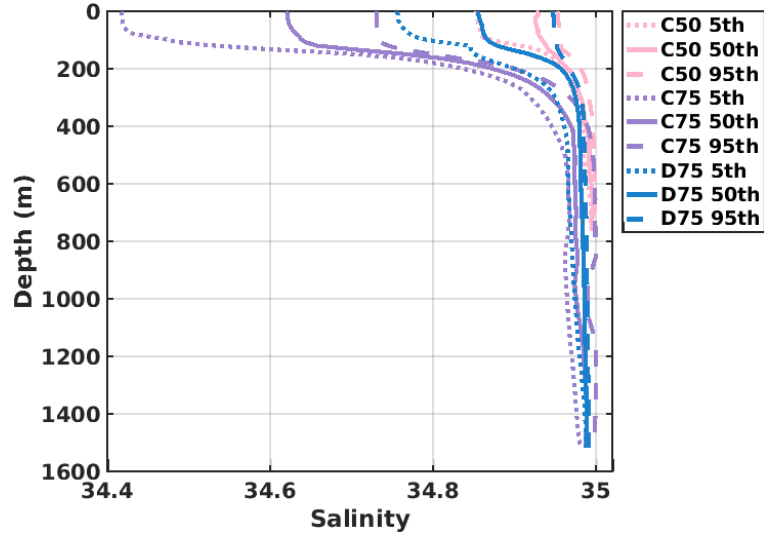


d. D75

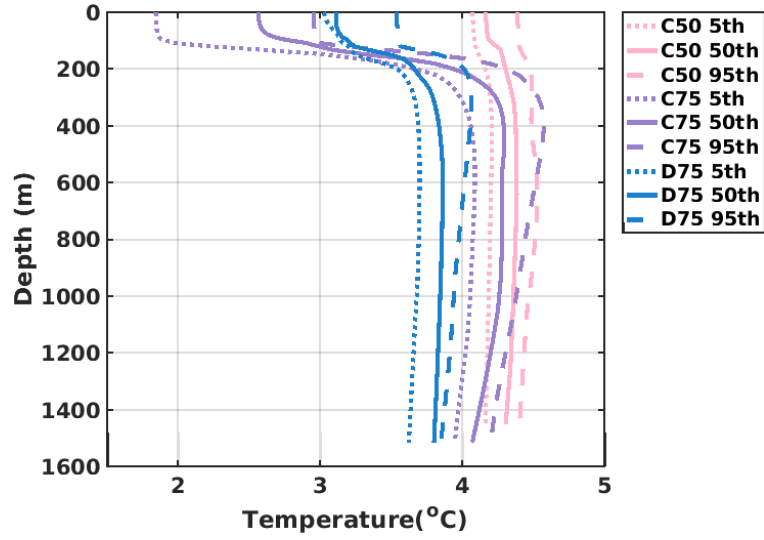


e. D75-C75

Figure 4: Convective resistance (also known as the vertical integral buoyancy anomaly to be removed) averaged over the period 2012 - 2017 for the winter months of January to March; units are m^2/s^2 . Dashed black line shows 2000 m isobath and solid black line shows 3000 m isobath. Magenta lines show mixed layer depths of 400 m (dashed) and 1200 m (solid). Regions with bathymetry shallower than 2000 m are masked out of the figure. Each configuration is shown: (a) C50, (b) C75, (c) difference between C50 and C75, (d) D75, and (e) difference between D75 and C75.



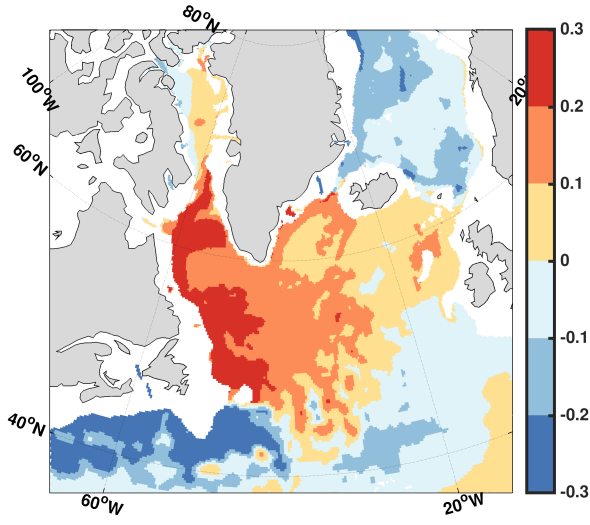
a.



b.

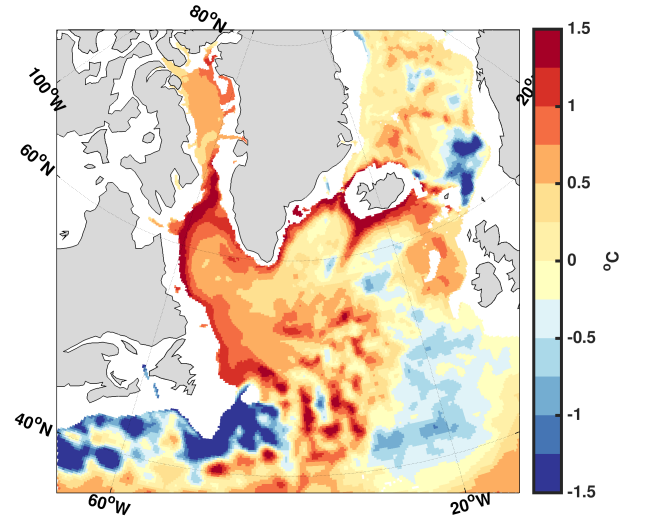
Figure 5: Potential temperature and salinity profile averaged for the interior of the Labrador Sea. The 5th, 50th, and 95th percentiles for each model fields are plotted for each experiment, of January to March of 2012 to 2017, within the top ~ 1500 m of the water column (1452.23 m in C50 and 1516.36 m for C75 and D75). Data points are excluded where $S < 32$, $S > 35$, or $T > 7^\circ\text{C}$.

Salinity

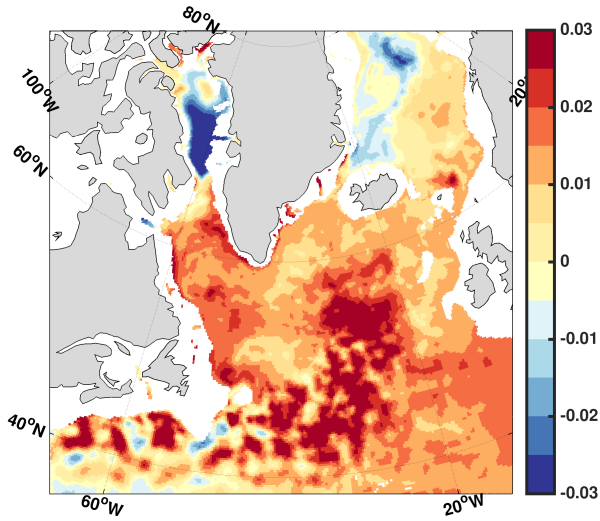


a. C50 - C75

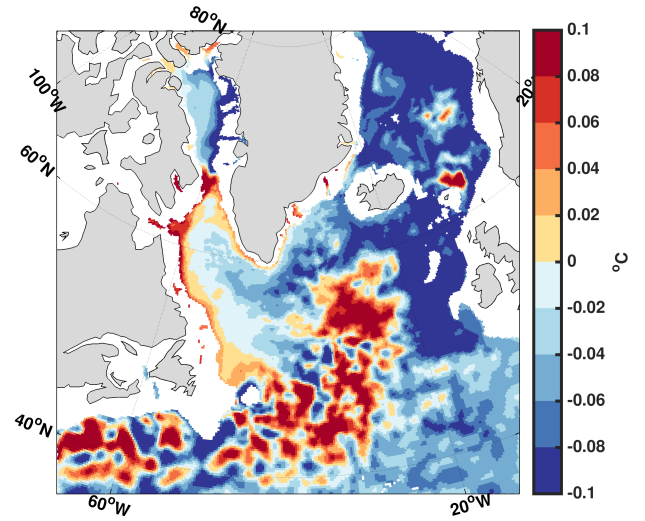
Temperature



b. C50 - C75

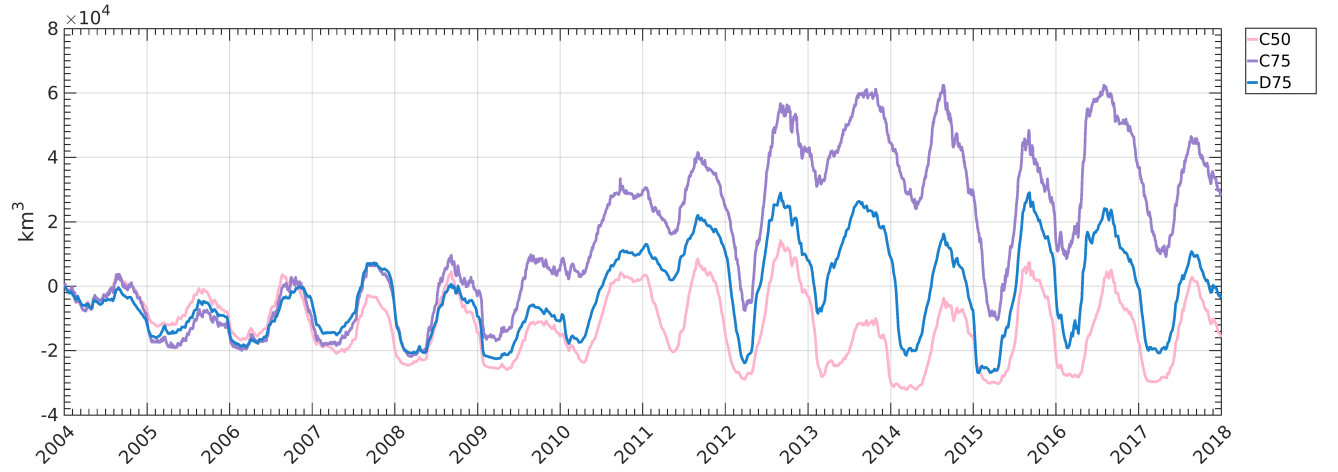


c. D75 - C75

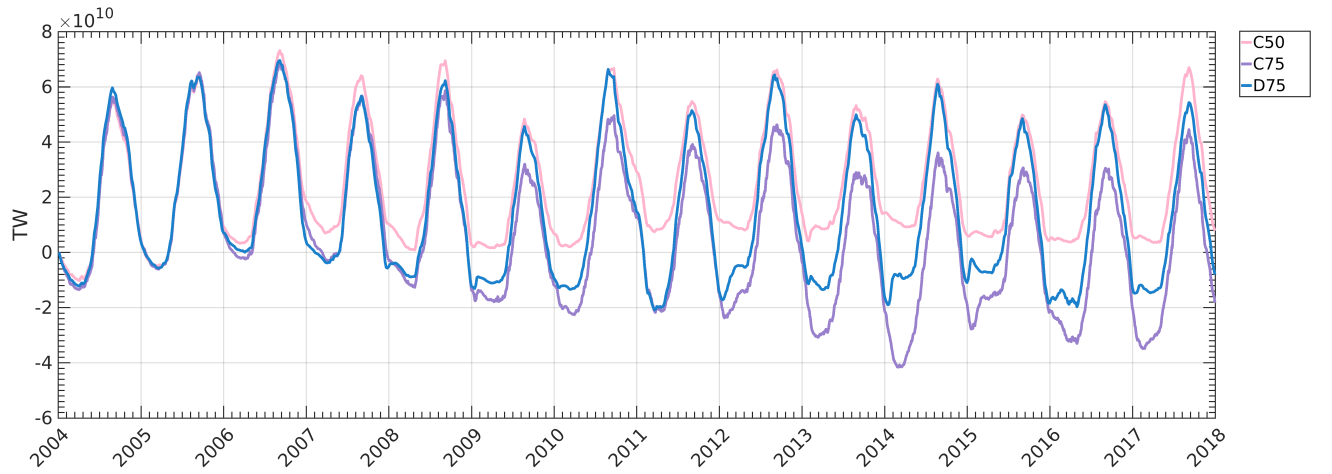


d. D75 - C75

Figure 6: Difference in wintertime (Jan.-March, 2012-2017) average salinity (left) and temperature (right) over the upper 450 m of the water column for C50-C75 (top) and D75-C75 (bottom).

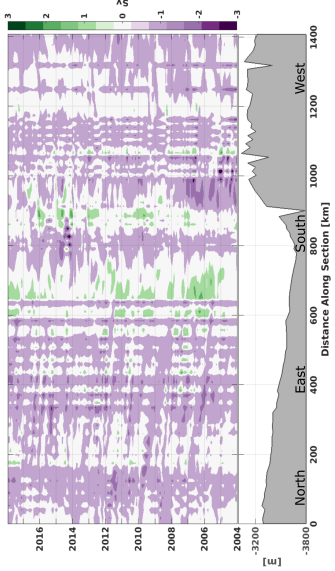


a. Freshwater Content

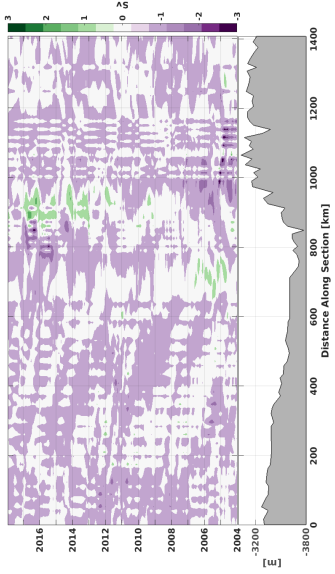


b. Heat Content

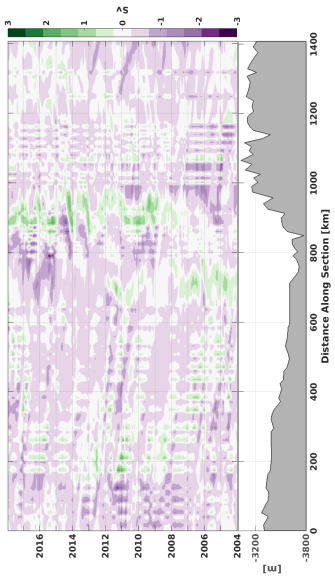
Figure 7: Interior of the Labrador Sea's freshwater (a) and heat content (b) over the top 1500 m of the water column (Equation 2 and Equation 3 with $S_{ref} = 34.97$ and $T_{ref} = 4^{\circ}C$). With a reference to the beginning of the time series; therefore, an anomaly from the start's state is shown (5 day average at the start of January 2004).



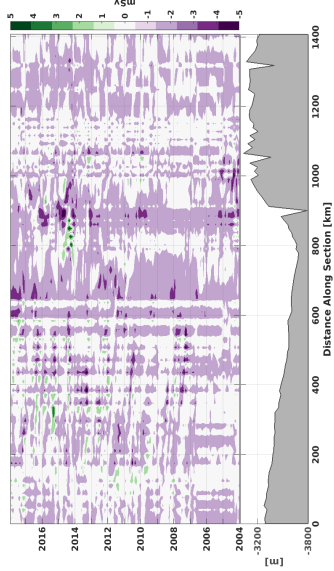
a. C50 Volume Flux



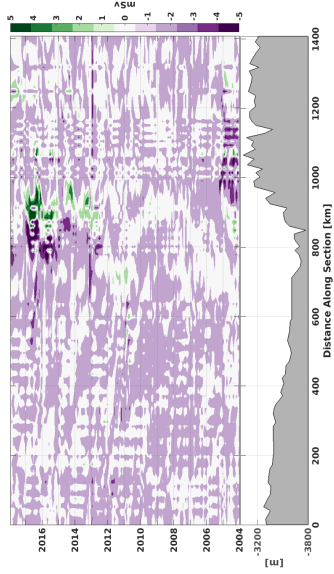
b. C75 Volume Flux



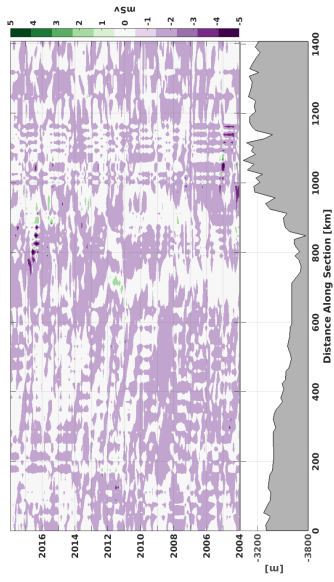
c. D75 Volume Flux



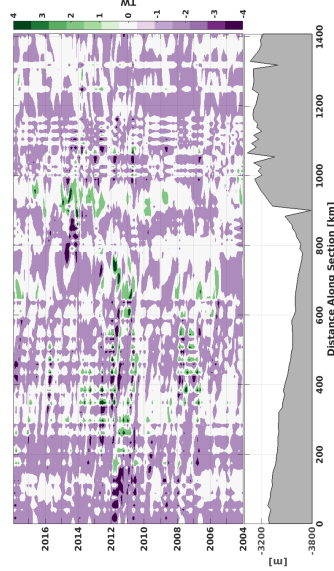
d. C50 Freshwater Flux



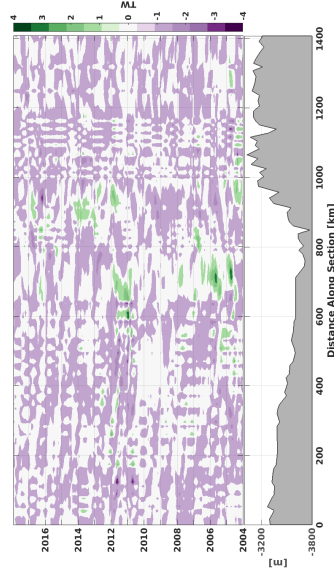
e. C75 Freshwater Flux



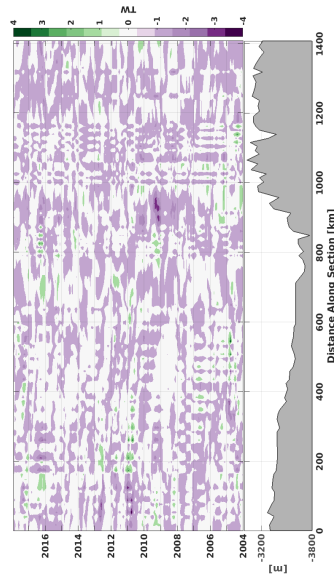
f. D75 Freshwater Flux



g. C50 Temperature Flux

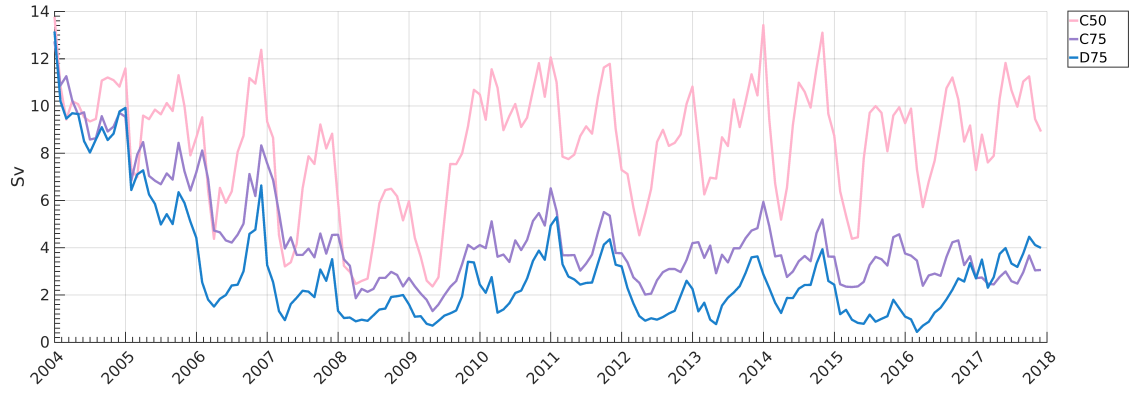


h. C75 Temperature Flux

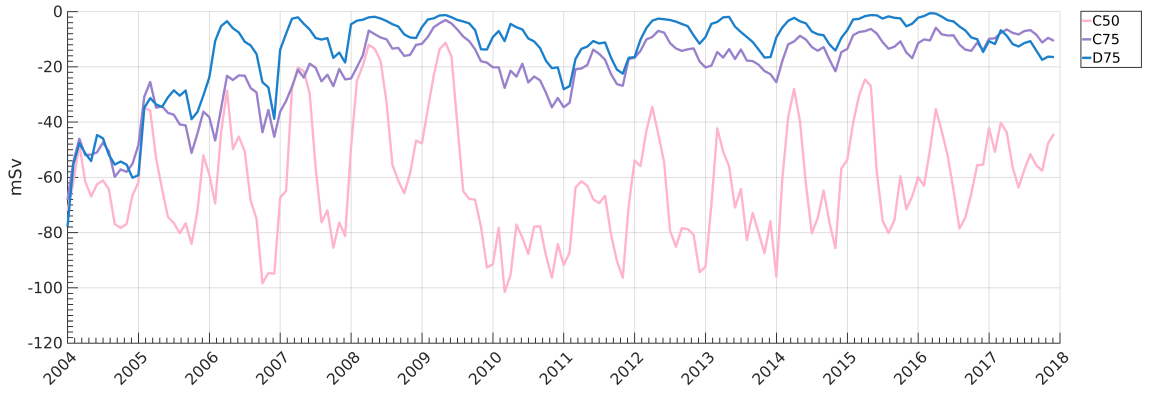


i. D75 Temperature Flux

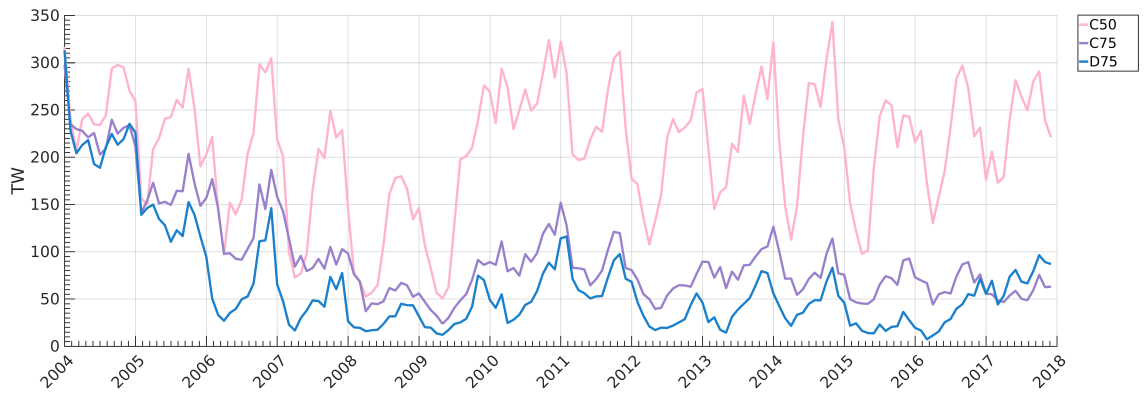
Figure 8: Monthly averaged fluxes into (positive) and out of (negative) the interior of the Labrador Sea (into and out of the page, respectively). Fluxes are taken by the summation of the water column from 0 to 1500 m along the section using Equations 4 and 5. Distance markers along the section on the x-axis can be seen in Figure 1. A comparison of changing the vertical levels and atmospheric forcing is shown with C50 as the left column, C75 as the centre column, and D75 on the right column. Each row shows a different type of flux; the first row shows volume flux in Sv, the second row shows freshwater flux in mSv, and the third row shows temperature flux in TW.



a.

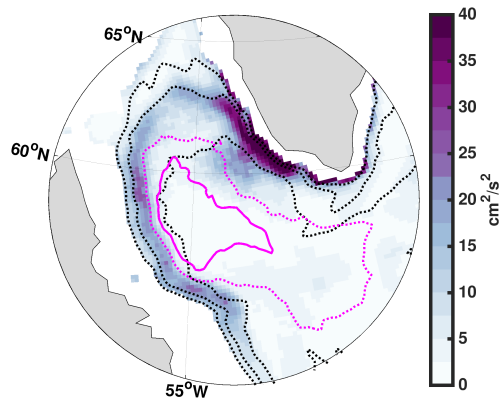


b.

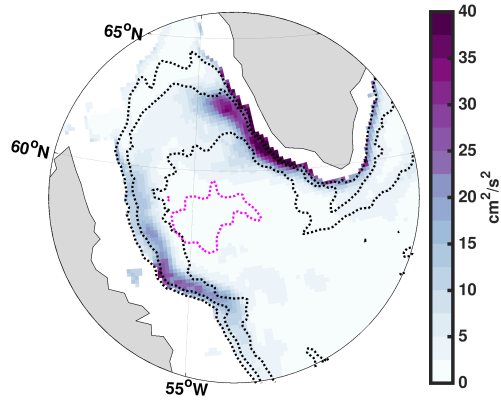


c.

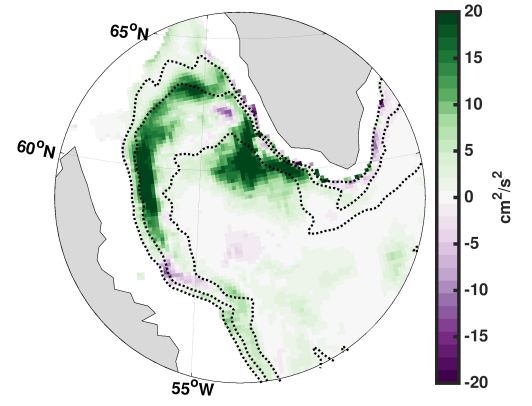
Figure 9: Irisinger Water fluxes at Cape Farewell (location shown in Figure 1) of volume (a), freshwater (b), and heat (c). Positive values indicate flux direction to the west. The reference salinity is $S_{ref} = 34.8$ (Aagaard and Carmack, 1989) and the reference temperature is $T_{ref} = 0^{\circ}C$. Bounds for the water mass properties are $S > 34.8$ and $\rho < 27.68kg/m^3$.



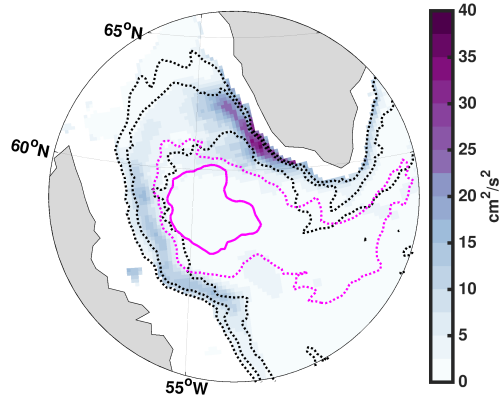
a. C50



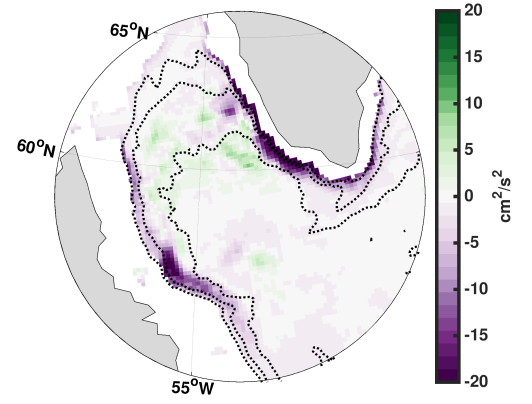
b. C75



c. C50 - C75

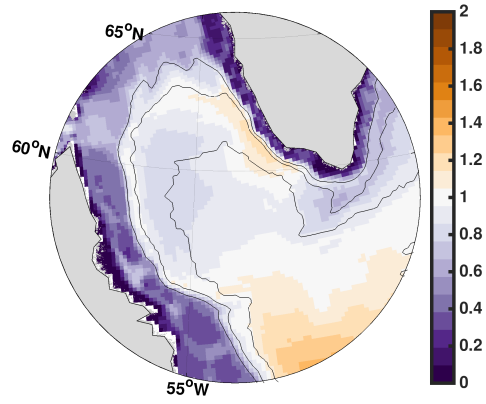


d. D75

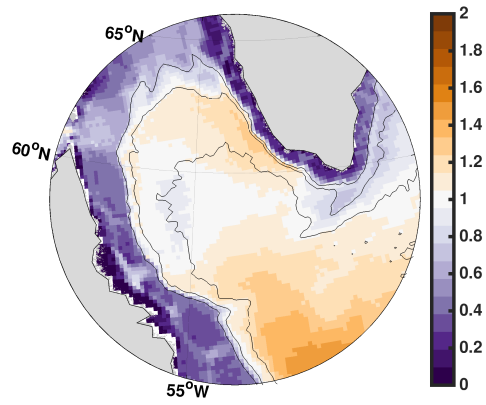


e. D75 - C75

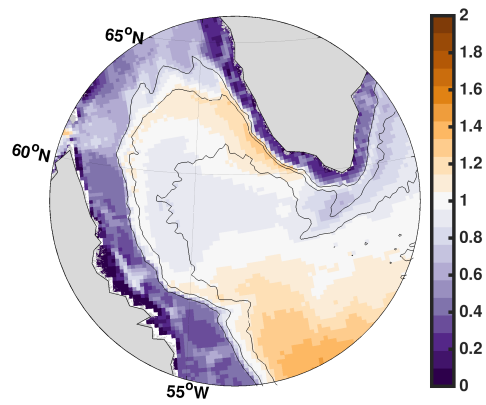
Figure 10: Average TKE of the top 500m of the water column for the winter months (January to March) of 2012 to 2017. Regions with bathymetry less than 500 m are masked out of the figure. Calculated using model velocities in Equation 6. Dashed black lines show depth contours of 1000 m, 2000 m, and 3000 m. Magenta lines show average mixed layer depths of 400 m (dashed) and 1200 m (solid). Each experiment is shown: (a) C50, (c) C75, (c) difference between C50 and C75, (d) D75, and (e) difference between D75 and C75.



a. C50



b. C75



c. D75

Figure 11: First baroclinic Rossby radius of deformation per model grid point over 2004-2017. A value greater than one means the deformation radius is larger (orange); therefore, can be resolved better.

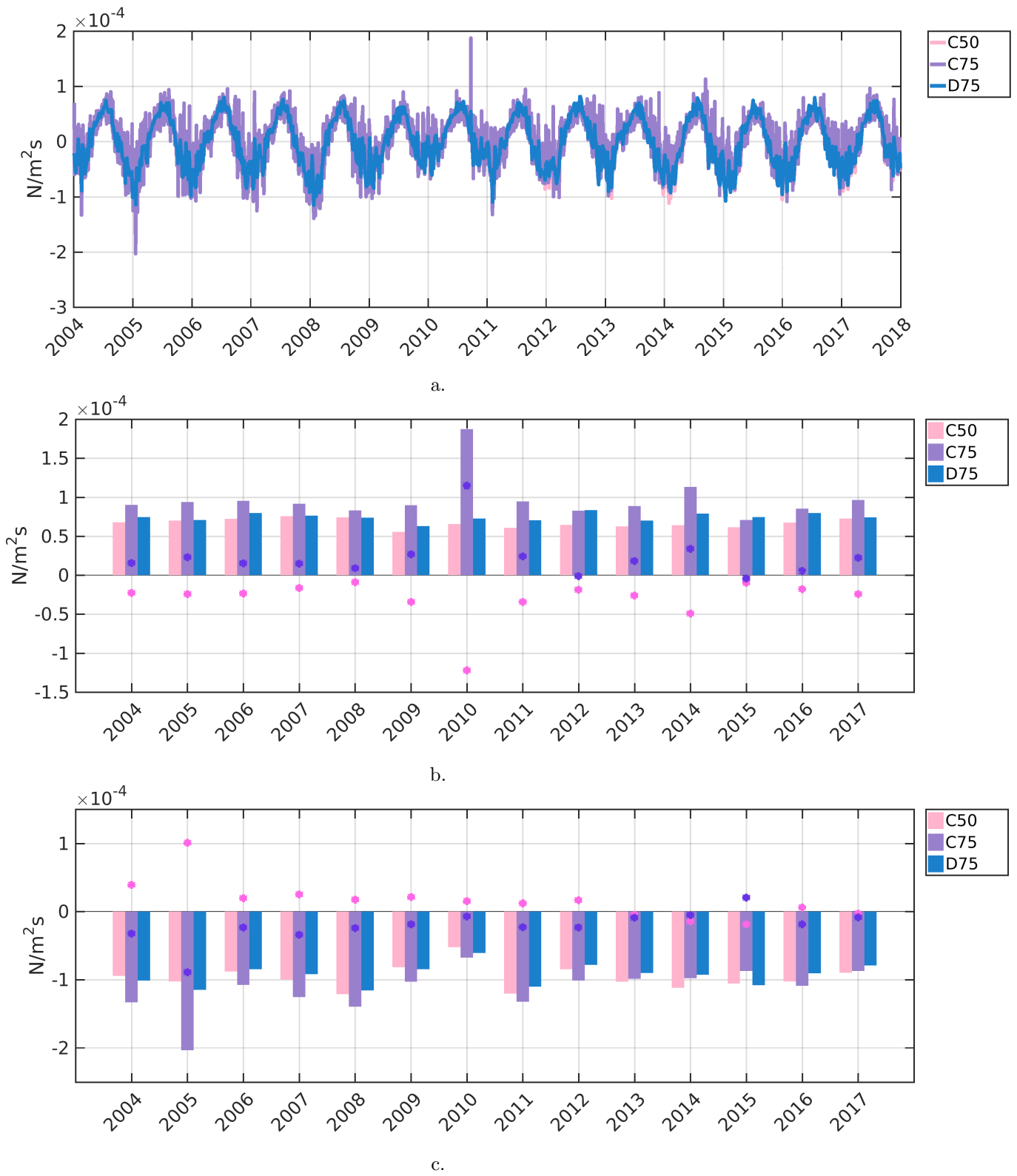


Figure 12: (a) Buoyancy flux from the atmosphere to the ocean surface calculated using Equation 7, averaged over the interior of the Labrador Sea (Figure 1). This figure shows a comparison of the three experiments with C50 in pink, C75 in purple and D75 in blue. Positive numbers indicate a gain in buoyancy in the ocean surface layer and negative values indicate a loss of buoyancy (denser) in the surface layer. (b) maximum gain of buoyancy by ocean surface each year, with asterisk symbols indicating the difference between C50-C75 in bright pink and C75-D75 in dark purple. (c) same from (b) with maximum loss of buoyancy each year.

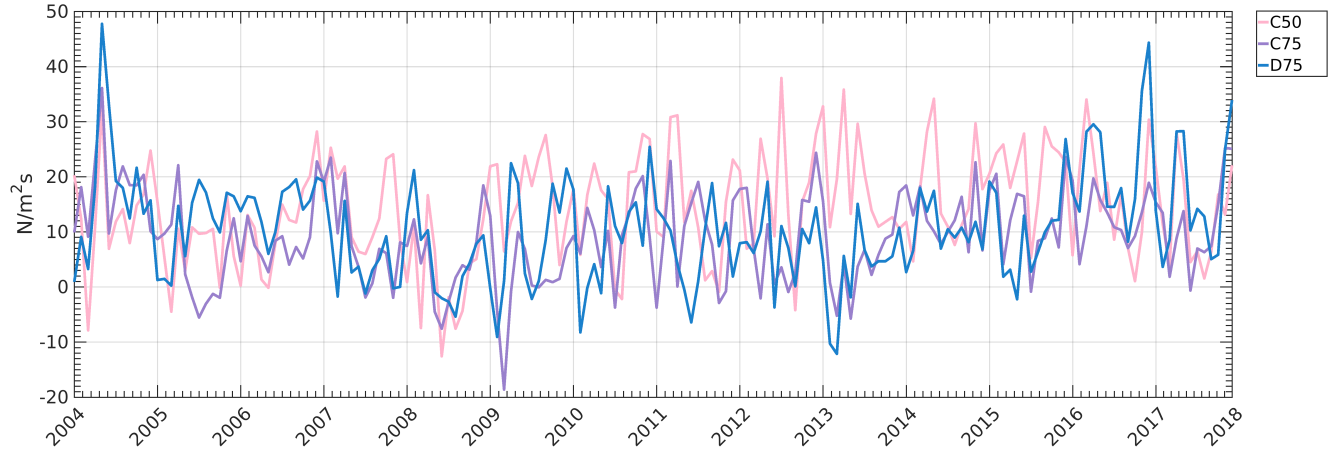


Figure 13: Lateral buoyancy flux of the interior of the Labrador Sea (Figure 1) inferred from Equation 7 while integrating over the surface area of the lateral boundaries of the convection region. This figure shows the monthly average comparison of the three experiments with C50 in pink, C75 in purple and D75 in blue. Positive numbers indicate a gain in buoyancy in the interior of the Labrador Sea and negative values indicate a loss of buoyancy (denser).

References

- Aagaard, K., Carmack, E.C., 1989. The role of sea ice and other fresh water in
770 the Arctic circulation. *Journal of Geophysical Research: Oceans* 94, 14485–
14498. doi:10.1029/JC094iC10p14485.
- Amante, C., Eakins, B., 2009. ETOPO1 1 Arc-Minute Global Relief Model: Pro-
cedures, Data Sources and Analysis. NOAA Technical Memorandum NESDIS
NGDC-24 doi:10.7289/V5C8276M.
- 775 Bailey, D.A., Rhines, P.B., Häkkinen, S., 2005. Formation and pathways
of North Atlantic Deep Water in a coupled ice–ocean model of the Arc-
tic–North Atlantic Oceans. *Climate Dynamics* 25, 497–516. doi:10.1007/
s00382-005-0050-3.
- Bamber, J.L., Tedstone, A.J., King, M.D., Howat, I.M., Enderlin,
780 E.M., van den Broeke, M.R., Noel, B., 2018. Land Ice Fresh-
water Budget of the Arctic and North Atlantic Oceans: 1. Data,
Methods, and Results. *Journal of Geophysical Research: Oceans*
123, 1827–1837. URL: <https://agupubs.onlinelibrary.wiley.com/doi/abs/10.1002/2017JC013605>,
doi:10.1002/2017JC013605,
785 arXiv:<https://agupubs.onlinelibrary.wiley.com/doi/pdf/10.1002/2017JC013605>.
- Barnier, B., Brodeau, L., Le Sommer, J., Molines, J.M., Penduff, T., Theetten,
S., Tréguier, A.M., Madec, G., Biastoch, A., Böning, C.W., Dengg, J., Gulev,
S.K., Bourdallé-Badie, R., Chanut, J., Garric, G., Alderson, S., Coward,
A.C., De Cuevas, B., New, A.L., Haines, K., Smith, G.C., Drijfhout, S.,
790 Hazeleger, W., Severijns, C.A., Myers, P.G., 2007. Eddy-permitting ocean
circulation hindcasts of past decades. *CLIVAR Exchanges* 12, 8–10. URL:
<https://hal.archives-ouvertes.fr/hal-00266990>.
- Barnier, B., Madec, G., Penduff, T., Molines, J.M., Treguier, A.M., Sommer,
J., Beckmann, A., Böning, C., Dengg, J., Derval, C., Durand, E., Gulev, S.,
795 Remy, E., Talandier, C., Theetten, S., Maltrud, M., Mcclean, J., Cuevas, B.,

2006. Impact of partial steps and momentum advection schemes in a global ocean circulation model at eddy-permitting resolution. *Ocean Dynamics* 56.
- Bernard, B., Madec, G., Penduff, T., Molines, J.M., Treguier, A.M., Le Sommer, J., Beckmann, A., Biastoch, A., Böning, C., Dengg, J., Derval, C.,
800 Durand, E., Gulev, S., Remy, E., Talandier, C., Theetten, S., Maltrud, M., McClean, J., De Cuevas, B., 2006. Impact of partial steps and momentum advection schemes in a global ocean circulation model at eddy-permitting resolution. *Ocean Dynamics* 56, 543–567. URL: <https://doi.org/10.1007/s10236-006-0082-1>, doi:10.1007/s10236-006-0082-1.
- 805 Bigg, G.R., Wadley, M.R., Stevens, D.P., Johnson, J.A., 1997. Modelling the dynamics and thermodynamics of icebergs. *Cold Regions Science and Technology* 26, 113 – 135. URL: <http://www.sciencedirect.com/science/article/pii/S0165232X97000128>, doi:[https://doi.org/10.1016/S0165-232X\(97\)00012-8](https://doi.org/10.1016/S0165-232X(97)00012-8).
- 810 BODC, 2008. British Oceanographic Data Center’s General Bathymetric Chart of the Oceans. http://www.gebco.net/data_and_products/gridded_bathymetry_data/.
- Böning, C.W., Behrens, E., Biastoch, A., Getzlaff, K., Bamber, J.L., 2016. Emerging impact of Greenland meltwater on deepwater formation in the
815 North Atlantic Ocean. *Nature Geosci* 9, 523–527. doi:10.1038/ngeo2740.
- Chanut, J., Barnier, B., Large, W., Debreu, L., Penduff, T., Molines, J.M., Mathiot, P., 2008. Mesoscale Eddies in the Labrador Sea and Their Contribution to Convection and Restratication. *Journal of Physical Oceanography* 38, 1617–1643. URL: <https://doi.org/10.1175/2008JP03485.1>, doi:10.1175/2008JP03485.1, arXiv:<https://doi.org/10.1175/2008JP03485.1>.
820
- Colombo, P., Barnier, B., Penduff, T., Chanut, J., Deshayes, J., Molines, J.M., Sommer, J., Verezemskaya, P., Gulev, S., Treguier, A.M., 2020. Representation of the Denmark Strait overflow in a z -coordinate eddying configuration

- of the NEMO (v3.6) ocean model: resolution and parameter impacts. *Geoscientific Model Development* 13, 3347–3371. doi:10.5194/gmd-13-3347-2020.
- 825 Courtois, P., Hu, X., Pennelly, C., Spence, P., Myers, P.G., 2017. Mixed layer depth calculation in deep convection regions in ocean numerical models. *Ocean Modelling* 120, 60 – 78. URL: <http://www.sciencedirect.com/science/article/pii/S146350031730152X>,
830 doi:<https://doi.org/10.1016/j.ocemod.2017.10.007>.
- Cuny, J., Rhines, P.B., Niller, P.P., Bacon, S., 2002. Labrador sea boundary currents and the fate of the Irminger sea water. *Journal of Physical Oceanography* 32, 627. URL: [http://uml.idm.oclc.org/login?url=https://search.ebscohost.com/login.aspx?direct=true&db=a9h&AN=](http://uml.idm.oclc.org/login?url=https://search.ebscohost.com/login.aspx?direct=true&db=a9h&AN=6102711&site=ehost-live)
835 [6102711&site=ehost-live](http://uml.idm.oclc.org/login?url=https://search.ebscohost.com/login.aspx?direct=true&db=a9h&AN=6102711&site=ehost-live).
- Dai, A., Qian, T., Trenberth, K.E., Milliman, J.D., 2009. Changes in continental freshwater discharge from 1948 to 2004. *Journal of Climate* 22, 2773–2792.
- Dukhovskoy, D.S., Yashayaev, I., Proshutinsky, A., Bamber, J.L., Bashmachnikov, I.L., Chassignet, E.P., Lee, C.M., Tedstone, A.J., 2019.
840 Role of Greenland Freshwater Anomaly in the Recent Freshening of the Subpolar North Atlantic. *Journal of Geophysical Research: Oceans* 124, 3333–3360. URL: <https://agupubs.onlinelibrary.wiley.com/doi/abs/10.1029/2018JC014686>, doi:10.1029/2018JC014686, arXiv:<https://agupubs.onlinelibrary.wiley.com/doi/pdf/10.1029/2018JC014686>.
- 845 Dussin, R., Barnier, B., Brodeau, L., 2016. The making of Drakkar forcing set DFS5 Grenoble, 612 France: LGGE.
- Ferry, N., Greiner, E., Garric, G., Penduff, T., Treiguer, A.M., Reverdin, G., 2008. GLORYS-1 Reference Manual for Stream 1 (2002-2007). GLORYS project report.
- 850 Feucher, C., Garcia-Quintana, Y., Yashayaev, I., Hu, X., Myers, P.G., 2019. Labrador Sea Water Formation Rate and Its Impact on the

- Local Meridional Overturning Circulation. *Journal of Geophysical Research: Oceans* 124, 5654–5670. URL: <https://agupubs.onlinelibrary.wiley.com/doi/abs/10.1029/2019JC015065>, doi:10.1029/2019JC015065, 855 [arXiv:https://agupubs.onlinelibrary.wiley.com/doi/pdf/10.1029/2019JC015065](https://agupubs.onlinelibrary.wiley.com/doi/pdf/10.1029/2019JC015065).
- Fichefet, T., Morales Maqueda, M., 1997. Sensitivity of a global sea ice model to the treatment of ice thermodynamics and dynamics. *Journal of Geophysical Research* 102, 12609–12646.
- Frajka-Williams, E., Rhines, P.B., Eriksen, C.C., 2014. Horizontal 860 Stratification during Deep Convection in the Labrador Sea. *Journal of Physical Oceanography* 44, 220–228. URL: <https://doi.org/10.1175/JPO-D-13-069.1>, doi:10.1175/JPO-D-13-069.1, [arXiv:https://doi.org/10.1175/JPO-D-13-069.1](https://doi.org/10.1175/JPO-D-13-069.1).
- Fratantoni, D.M., 2001. North atlantic surface circulation during the 1990’s 865 observed with satellite-tracked drifters. *Journal of Geophysical Research: Oceans* 106, 22067–22093.
- Garcia-Quintana, Y., Courtois, P., Hu, X., Pennelly, C., Kieke, D., Myers, P.G., 2019. Sensitivity of Labrador Sea Water Formation to Changes in Model Resolution, Atmospheric Forcing, and Freshwater Input. *Journal of Geophysical Research: Oceans* 124, 2126–2152. URL: <https://agupubs.onlinelibrary.wiley.com/doi/abs/10.1029/2018JC014459>, doi:10.1029/2018JC014459, 870 [arXiv:https://agupubs.onlinelibrary.wiley.com/doi/pdf/10.1029/2018JC014459](https://agupubs.onlinelibrary.wiley.com/doi/pdf/10.1029/2018JC014459).
- Gelderloos, R., Katsman, C.A., Drijfhout, S.S., 2011. Assessing the Roles of Three Eddy Types in Restratifying the Labrador Sea after Deep 875 Convection. *Journal of Physical Oceanography* 41, 2102–2119. URL: <https://doi.org/10.1175/JPO-D-11-054.1>, doi:10.1175/JPO-D-11-054.1, [arXiv:https://doi.org/10.1175/JPO-D-11-054.1](https://doi.org/10.1175/JPO-D-11-054.1).
- Gill, A.E., 1982. *Atmosphere-Ocean Dynamics*, Academic Press, p. 662.

- Gillard, L.C., Hu, X., Myers, P.G., Bamber, J.L., 2016. Meltwater pathways
880 from marine terminating glaciers of the Greenland Ice Sheet. *Geophysical Research Letters* 43, 10,873–10,882. URL: <http://dx.doi.org/10.1002/2016GL070969>, doi:10.1002/2016GL070969.
- Gladstone, R.M., Bigg, G.R., Nicholls, K.W., 2001. Iceberg trajectory modeling and meltwater injection in the Southern Ocean. *Journal of Geophysical Research: Oceans* 106, 19903–19915. URL: <https://agupubs.onlinelibrary.wiley.com/doi/abs/10.1029/2000JC000347>, doi:10.1029/2000JC000347, arXiv:<https://agupubs.onlinelibrary.wiley.com/doi/pdf/10.1029/2000JC000347>.
- Hirschi, J.J.M., Barnier, B., Böning, C., Biastoch, A., Blaker, A.T., Coward, A., Danilov, S., Drijfhout, S., Getzlaff, K., Griffies, S.M., Hasumi, H.,
890 Hewitt, H., Iovino, D., Kawasaki, T., Kiss, A.E., Koldunov, N., Marzocchi, A., Mecking, J.V., Moat, B., Molines, J.M., Myers, P.G., Penduff, T., Roberts, M., Treguier, A.M., Sein, D.V., Sidorenko, D., Small, J., Spence, P., Thompson, L., Weijer, W., Xu, X., 2020. The Atlantic Meridional Overturning Circulation in High-Resolution Models. *Journal of Geophysical Research: Oceans* 125, e2019JC015522. URL: <https://agupubs.onlinelibrary.wiley.com/doi/abs/10.1029/2019JC015522>, doi:10.1029/2019JC015522, arXiv:<https://agupubs.onlinelibrary.wiley.com/doi/pdf/10.1029/2019JC015522>.
895 e2019JC015522 2019JC015522.
- Holdsworth, A.M., Myers, P.G., 2015. The influence of high-frequency
900 atmospheric forcing on the circulation and deep convection of the Labrador Sea. *Journal of Climate* 28, 4980–4996. URL: <https://doi.org/10.1175/JCLI-D-14-00564.1>, doi:10.1175/JCLI-D-14-00564.1, arXiv:<https://doi.org/10.1175/JCLI-D-14-00564.1>.
- Holte, J., Talley, L., 2009. A new algorithm for finding mixed layer depths with
905 applications to argo data and subantarctic mode water formation. *Journal of Atmospheric and Oceanic Technology - J ATMOS OCEAN TECHNOL* 26. doi:10.1175/2009JTECH0543.1.

- Holte, J., Talley, L.D., Gilson, J., Roemmich, D., 2017. An Argo mixed layer climatology and database. *Geophysical Research Letters* 44, 5618–5626. URL: <https://agupubs.onlinelibrary.wiley.com/doi/abs/10.1002/2017GL073426>, doi:<https://doi.org/10.1002/2017GL073426>, arXiv:<https://agupubs.onlinelibrary.wiley.com/doi/pdf/10.1002/2017GL073426>.
- IOC, SCOR, and IAPSO, 2010. The international thermodynamic equation of seawater - 2010 : Calculation and use of thermodynamic properties. Intergovernmental Oceanographic Commission, Manuals and Guides No. 56, UNESCO (English).
- de Jong, M.F., Bower, A.S., Furey, H.H., 2014. Two Years of Observations of Warm-Core Anticyclones in the Labrador Sea and Their Seasonal Cycle in Heat and Salt Stratification. *Journal of Physical Oceanography* 44, 427–444. URL: <https://doi.org/10.1175/JPO-D-13-070.1>, doi:10.1175/JPO-D-13-070.1, arXiv:<https://doi.org/10.1175/JPO-D-13-070.1>.
- Katsman, C.A., Spall, M.A., Pickart, R.S., 2004. Boundary Current Eddies and Their Role in the Restratification of the Labrador Sea. *Journal of Physical Oceanography* 34, 1967–1983. URL: [https://doi.org/10.1175/1520-0485\(2004\)034<1967:BCEATR>2.0.CO;2](https://doi.org/10.1175/1520-0485(2004)034<1967:BCEATR>2.0.CO;2), doi:10.1175/1520-0485(2004)034<1967:BCEATR>2.0.CO;2, arXiv:[https://doi.org/10.1175/1520-0485\(2004\)034<1967:BCEATR>2.0.CO;2](https://doi.org/10.1175/1520-0485(2004)034<1967:BCEATR>2.0.CO;2).
- Koenigk, T., Fuentes Franco, R., Meccia, V., Gutjahr, O., Jackson, L., New, A., Ortega, P., Roberts, C., Roberts, M., Arsouze, T., Iovino, D., Moine, M.P., Sein, D., 2021. Deep mixed ocean volume in the labrador sea in highresmip models. *Climate Dynamics* 57, 1895–1918. doi:10.1007/s00382-021-05785-x.
- Kuhlbrodt, T., Griesel, A., Montoya, M., Levermann, A., Hofmann, M., Rahmstorf, S., 2007. On the driving processes of the Atlantic Meridional Overturning Circulation. *Reviews of Geophysics* 45. URL: <https://agupubs.onlinelibrary.wiley.com/doi/abs/10.1029/2006RG000251>.

com/doi/abs/10.1029/2004RG000166, doi:10.1029/2004RG000166,
arXiv:https://agupubs.onlinelibrary.wiley.com/doi/pdf/10.1029/2004RG000166.

Large, W.G., Yeager, S.G., 2004. Diurnal to decadal global forcing for ocean
940 and sea-ice models: the datasets and flux climatologies .

Lau, N.C., 1988. Variability of the Observed Midlatitude Storm
Tracks in Relation to Low-Frequency Changes in the Circulation Pat-
tern. Journal of the Atmospheric Sciences 45, 2718–2743. URL:
https://doi.org/10.1175/1520-0469(1988)045<2718:VOTOMS>2.
945 0.CO;2, doi:10.1175/1520-0469(1988)045<2718:VOTOMS>2.0.CO;2,
arXiv:https://doi.org/10.1175/1520-0469(1988)045<2718:VOTOMS>2.0.CO;2.

Lazier, J.R., 1980. Oceanographic conditions at ocean weather ship bravo,
1964–1974. Atmosphere-Ocean 18, 227–238. URL: https://doi.org/
10.1080/07055900.1980.9649089, doi:10.1080/07055900.1980.9649089,
950 arXiv:https://doi.org/10.1080/07055900.1980.9649089.

Lozier, M.S., Li, F., Bacon, S., Bahr, F., Bower, A.S., Cunningham,
S.A., de Jong, M.F., de Steur, L., deYoung, B., Fischer, J., Gary, S.F.,
Greenan, B.J.W., Holliday, N.P., Houk, A., Houpert, L., Inall, M.E.,
Johns, W.E., Johnson, H.L., Johnson, C., Karstensen, J., Koman, G.,
955 Le Bras, I.A., Lin, X., Mackay, N., Marshall, D.P., Mercier, H., Olt-
manns, M., Pickart, R.S., Ramsey, A.L., Rayner, D., Straneo, F., Thierry,
V., Torres, D.J., Williams, R.G., Wilson, C., Yang, J., Yashayaev, I.,
Zhao, J., 2019. A sea change in our view of overturning in the sub-
polar North Atlantic. Science 363, 516–521. URL: https://science.
960 sciencemag.org/content/363/6426/516, doi:10.1126/science.aau6592,
arXiv:https://science.sciencemag.org/content/363/6426/516.full.pdf.

Luo, H., Castelao, R.M., Rennermalm, A.K., Tedesco, M., Bracco, A., Yager,
P.L., Mote, T.L., 2016. Oceanic transport of surface meltwater from the
southern Greenland Ice Sheet. Nature Geoscience doi:10.1038/ngeo2708.

- 965 MacGilchrist, G.A., Johnson, H.L., Marshall, D.P., Lique, C., Thomas, M.,
Jackson, L.C., Wood, R.A., 2020. Locations and Mechanisms of Ocean
Ventilation in the High-Latitude North Atlantic in an Eddy-Permitting
Ocean Model. *Journal of Climate* 33. URL: [https://doi.org/10.1175/
JCLI-D-20-0191.1](https://doi.org/10.1175/JCLI-D-20-0191.1).
- 970 Madec, G., 2008. NEMO ocean engine. Note du Pole de modélisation .
- Marsh, R., Ivchenko, V.O., Skliris, N., Alderson, S., Bigg, G.R., Madec, G.,
Blaker, A.T., Aksenov, Y., Sinha, B., Coward, A.C., Le Sommer, J., Merino,
N., Zalesny, V.B., 2015. NEMO-ICB (v1.0): interactive icebergs in the NEMO
ocean model globally configured at eddy-permitting resolution. *Geoscientific
975 Model Development* 8, 1547–1562. URL: [https://www.geosci-model-dev.
net/8/1547/2015/](https://www.geosci-model-dev.net/8/1547/2015/), doi:10.5194/gmd-8-1547-2015.
- Marshall, J., Dobson, F., Moore, K., Rhines, P., Visbeck, M., D’Asaro, E.,
Bumke, K., Chang, S., Davis, R., Fischer, K., Garwood, R., Guest, P., Har-
court, R., Herbaut, C., Holt, T., Lazier, J., Legg, S., McWilliams, J., Pickart,
980 R., Prater, M., Renfrew, I., Schott, F., Send, U., Smethie, W., 1998. The
Labrador Sea Deep Convection Experiment. *Bulletin of the American Mete-
orological Society* 79, 2033–2058.
- Marson, J.M., Myers, P.G., Hu, X., Le Sommer, J., 2018. Using
Vertically Integrated Ocean Fields to Characterize Greenland Ice-
985 bergs’ Distribution and Lifetime. *Geophysical Research Letters*
45, 4208–4217. URL: [https://agupubs.onlinelibrary.wiley.
com/doi/abs/10.1029/2018GL077676](https://agupubs.onlinelibrary.wiley.com/doi/abs/10.1029/2018GL077676), doi:10.1029/2018GL077676,
arXiv:<https://agupubs.onlinelibrary.wiley.com/doi/pdf/10.1029/2018GL077676>.
- Martin, T., Adcroft, A., 2010. Parameterizing the fresh-water flux
990 from land ice to ocean with interactive icebergs in a coupled cli-
mate model. *Ocean Modelling* 34, 111 – 124. URL: [http:
//www.sciencedirect.com/science/article/pii/S146350031000065X](http://www.sciencedirect.com/science/article/pii/S146350031000065X),
doi:<https://doi.org/10.1016/j.ocemod.2010.05.001>.

- Marzocchi, A., Hirschi, J., Holliday, N., Cunningham, S., Blaker, A., Cow-
 995 ard, A., 2015. The north atlantic subpolar circulation in an eddy-resolving
 global ocean model. *Journal of Marine Systems* 142, 126–143. doi:10.1016/
 j.jmarsys.2014.10.007.
- Masina, S., Storto, A., Storto, A., Ferry, N., Valdivieso, M., Haines, K.,
 Balmaseda, M., Zuo, H., Drevillon, M., Parent, L., 2017. An en-
 1000 semble of eddy-permitting global ocean reanalyses from the MyOcean
 project. *Climate Dynamics* 49, 813–841. URL: <https://doi.org/10.1007/s00382-015-2728-5>, doi:10.1007/s00382-015-2728-5.
- McCartney, M.S., Talley, L.D., 1982. The subpolar mode water
 of the north atlantic ocean. *Journal of Physical Oceanography*
 1005 12, 1169 – 1188. URL: [https://journals.ametsoc.org/view/](https://journals.ametsoc.org/view/journals/phoc/12/11/1520-0485_1982_012_1169_tsmwot_2_0_co_2.xml)
journals/phoc/12/11/1520-0485_1982_012_1169_tsmwot_2_0_co_2.xml,
 doi:10.1175/1520-0485(1982)012<1169:TSMWOT>2.0.CO;2.
- Merino, N., Sommer, J.L., Durand, G., Jourdain, N.C., Madec, G., Math-
 iot, P., Tournadre, J., 2016. Antarctic icebergs melt over the South-
 1010 ern Ocean: Climatology and impact on sea ice. *Ocean Modelling*
 104, 99 – 110. URL: [http://www.sciencedirect.com/science/article/](http://www.sciencedirect.com/science/article/pii/S1463500316300300)
[pii/S1463500316300300](http://www.sciencedirect.com/science/article/pii/S1463500316300300), doi:[https://doi.org/10.1016/j.ocemod.2016.](https://doi.org/10.1016/j.ocemod.2016.05.001)
 05.001.
- Morlighem, M., Williams, C.N., Rignot, E., An, L., Arndt, J.E., Bam-
 1015 ber, J.L., Catania, G., Chauché, N., Dowdeswell, J.A., Dorschel, B.,
 Fenty, I., Hogan, K., Howat, I., Hubbard, A., Jakobsson, M., Jordan,
 T.M., Kjeldsen, K.K., Millan, R., Mayer, L., Mouginot, J., Noël, B.P.Y.,
 O’Cofaigh, C., Palmer, S., Rysgaard, S., Seroussi, H., Siegert, M.J.,
 Slabon, P., Straneo, F., van den Broeke, M.R., Weinrebe, W., Wood,
 1020 M., Zinglensen, K.B., 2017. BedMachine v3: Complete Bed Topography
 and Ocean Bathymetry Mapping of Greenland From Multibeam Echo
 Sounding Combined With Mass Conservation. *Geophysical Research*

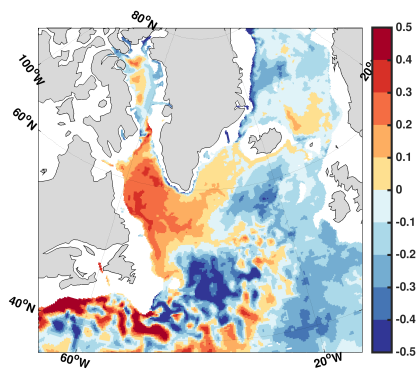
- Letters 44, 11,051–11,061. URL: <https://agupubs.onlinelibrary.wiley.com/doi/abs/10.1002/2017GL074954>, doi:10.1002/2017GL074954,
1025 arXiv:<https://agupubs.onlinelibrary.wiley.com/doi/pdf/10.1002/2017GL074954>.
- Myers, P., Kulan, N., Ribergaard, M., 2007. Irminger Water variability in the West Greenland Current. *Geophys. Res. Lett.* 34. doi:10.1029/2007GL030419.
- Pennelly, C., Hu, X., Myers, P.G., 2019. Cross-Isobath Freshwater Exchange Within the North Atlantic Subpolar Gyre. *Journal of Geophysical Research: Oceans* 124, 6831–6853. URL: <https://agupubs.onlinelibrary.wiley.com/doi/abs/10.1029/2019JC015144>, doi:10.1029/2019JC015144,
1030 arXiv:<https://agupubs.onlinelibrary.wiley.com/doi/pdf/10.1029/2019JC015144>.
- Pennelly, C., Myers, P.G., 2021. Impact of different atmospheric forcing sets on modeling labrador sea water production. *Journal of Geophysical Research: Oceans* 126, e2020JC016452. URL: <https://agupubs.onlinelibrary.wiley.com/doi/abs/10.1029/2020JC016452>,
1035 doi:<https://doi.org/10.1029/2020JC016452>, arXiv:<https://agupubs.onlinelibrary.wiley.com/doi/pdf/10.1029/2020JC016452>. e2020JC016452 2020JC016452.
- Petit, T., Lozier, M.S., Josey, S.A., Cunningham, S.A., 2020. Atlantic deep water formation occurs primarily in the iceland basin and irvinger sea by local buoyancy forcing. *Geophysical research letters* 47.
1040
- Rabe, B., Karcher, M., Kauker, F., Schauer, U., Toole, J.M., Krishfield, R.A., Pisarev, S., Kikuchi, T., Su, J., 2014. Arctic Ocean basin liquid freshwater storage trend 1992–2012. *Geophysical Research Letters* 41, 961–968. URL: <https://agupubs.onlinelibrary.wiley.com/doi/abs/10.1002/2013GL058121>, doi:10.1002/2013GL058121,
1045 arXiv:<https://agupubs.onlinelibrary.wiley.com/doi/pdf/10.1002/2013GL058121>.
- Rattan, S., Myers, P.G., Treguier, A., Theetten, S., Biastoch, A., Böning, C., 2010. Towards an understanding of Labrador Sea salinity drift in eddy-permitting simulations. *Ocean Modelling* 35, 77–88.
1050

- Rhein, M., Steinfeldt, R., Huhn, O., Sültenfuß, J., Breckenfelder, T., 2018. Greenland Submarine Melt Water Observed in the Labrador and Irminger Sea. *Geophysical Research Letters* 45, 10,570–10,578. URL: <https://agupubs.onlinelibrary.wiley.com/doi/abs/10.1029/2018GL079110>, doi:10.1029/2018GL079110, arXiv:<https://agupubs.onlinelibrary.wiley.com/doi/pdf/10.1029/2018GL079110>.
- Rhein, M., Steinfeldt, R., Kieke, D., Stendardo, I., Yashayaev, I., 2017. Ventilation variability of Labrador Sea Water and its impact on oxygen and anthropogenic carbon: a review. *Philosophical Transactions of the Royal Society A: Mathematical, Physical and Engineering Sciences* 375, 20160321. URL: <https://royalsocietypublishing.org/doi/abs/10.1098/rsta.2016.0321>, doi:10.1098/rsta.2016.0321, arXiv:<https://royalsocietypublishing.org/doi/pdf/10.1098/rsta.2016.0321>.
- Rieck, J., Böning, C., Getzlaff, K., 2019. The Nature of Eddy Kinetic Energy in the Labrador Sea: Different Types of Mesoscale Eddies, Their Temporal Variability, and Impact on Deep Convection. *Journal of Physical Oceanography* 49. doi:10.1175/jpo-d-18-0243.1.
- Sathiyamoorthy, S., Moore, G.W.K., 2002. Buoyancy Flux at Ocean Weather Station Bravo. *Journal of Physical Oceanography* 32, 458–474. URL: [https://doi.org/10.1175/1520-0485\(2002\)032<0458:BFAOWS>2.0.CO;2](https://doi.org/10.1175/1520-0485(2002)032<0458:BFAOWS>2.0.CO;2), doi:10.1175/1520-0485(2002)032<0458:BFAOWS>2.0.CO;2, arXiv:[https://doi.org/10.1175/1520-0485\(2002\)032<0458:BFAOWS>2.0.CO;2](https://doi.org/10.1175/1520-0485(2002)032<0458:BFAOWS>2.0.CO;2).
- Schulze, L.M., Pickart, R.S., Moore, G.W.K., 2016. Atmospheric forcing during active convection in the Labrador Sea and its impact on mixed-layer depth. *Journal of Geophysical Research: Oceans* 121, 6978–6992. URL: <https://agupubs.onlinelibrary.wiley.com/doi/abs/10.1002/2015JC011607>, doi:10.1002/2015JC011607, arXiv:<https://agupubs.onlinelibrary.wiley.com/doi/pdf/10.1002/2015JC011607>.
- Schulze Chretien, L.M., Frajka-Williams, E., 2018. Wind-driven transport of

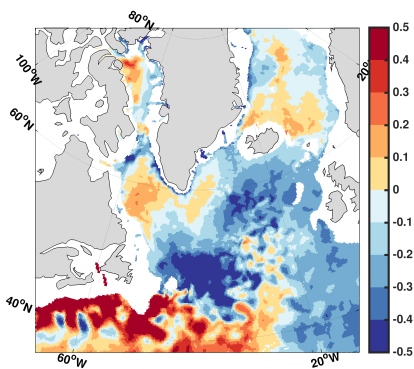
- fresh shelf water into the upper 30 m of the Labrador Sea. *Ocean Science* 14, 1247–1264. URL: <https://www.ocean-sci.net/14/1247/2018/>, doi:10.5194/os-14-1247-2018.
- Smith, G.C., Roy, F., Mann, P., Dupont, F., Brasnett, B., Lemieux, J.F.,
1085 Laroche, S., Bélair, S., 2014. A new atmospheric dataset for forcing ice-ocean models: Evaluation of reforecasts using the Canadian global deterministic prediction system. *Quarterly Journal of the Royal Meteorological Society* 140, 881–894.
- de Steur, L., Peralta-Ferriz, C., Pavlova, O., 2018. Freshwater Export in
1090 the East Greenland Current Freshens the North Atlantic. *Geophysical Research Letters* 45, 13,359–13,366. URL: <https://agupubs.onlinelibrary.wiley.com/doi/abs/10.1029/2018GL080207>, doi:10.1029/2018GL080207, arXiv:<https://agupubs.onlinelibrary.wiley.com/doi/pdf/10.1029/2018GL080207>.
- Stewart, K., Hogg, A., Griffies, S., Heerdegen, A., Ward, M.,
1095 Spence, P., England, M., 2017. Vertical resolution of baroclinic modes in global ocean models. *Ocean Modelling* 113, 50 – 65. URL: <http://www.sciencedirect.com/science/article/pii/S1463500317300434>, doi:<https://doi.org/10.1016/j.ocemod.2017.03.012>.
- Straneo, F., 2006. Heat and freshwater transport through the central Labrador
1100 Sea. *Journal of Physical Oceanography* 36, 606–628.
- Talley, L.D., Reid, J.L., Robbins, P.E., 2003. Data-Based Meridional Overturning Streamfunctions for the Global Ocean. *Journal of Climate* 16, 3213–3226. URL: [https://doi.org/10.1175/1520-0442\(2003\)016<3213:DMOSFT>2.0.CO;2](https://doi.org/10.1175/1520-0442(2003)016<3213:DMOSFT>2.0.CO;2),
1105 doi:10.1175/1520-0442(2003)016<3213:DMOSFT>2.0.CO;2, arXiv:[https://doi.org/10.1175/1520-0442\(2003\)016<3213:DMOSFT>2.0.CO;2](https://doi.org/10.1175/1520-0442(2003)016<3213:DMOSFT>2.0.CO;2).
- Treguier, A.M., Theetten, S., Chassignet, E.P., Penduff, T., Smith, R., Talley, L., Beismann, J.O., Böning, C., 2005. The North Atlantic Subpolar Gyre

- in Four High-Resolution Models. *Journal of Physical Oceanography* 35, 757–
1110 774. URL: <https://doi.org/10.1175/JP02720.1>, doi:10.1175/JP02720.1,
arXiv:<https://doi.org/10.1175/JP02720.1>.
- Våge, K., Pickart, R.S., Thierry, V., Reverdin, G., Lee, C.M., Petrie, B., Agnew,
T.A., Wong, A., Ribergaard, M.H., 2009. Surprising return of deep convection
to the subpolar North Atlantic Ocean in winter 2007–2008. *Nature Geoscience*
1115 2, 67–72. doi:10.1038/ngeo382.
- Wong, A.P.S., Wijffels, S.E., Riser, S.C., Pouliquen, S., Hosoda, S., Roem-
mich, D., Gilson, J., Johnson, G.C., Martini, K., Murphy, D.J., Scander-
beg, M., Bhaskar, T.V.S.U., Buck, J.J.H., Merceur, F., Carval, T., Maze,
G., Cabanes, C., André, X., Poffa, N., Yashayaev, I., Barker, P.M., Guine-
1120 hut, S., Belbéoch, M., Ignaszewski, M., Baringer, M.O., Schmid, C., Lyman,
J.M., McTaggart, K.E., Purkey, S.G., Zilberman, N., Alkire, M.B., Swift, D.,
Owens, W.B., Jayne, S.R., Hersh, C., Robbins, P., West-Mack, D., Bahr, F.,
Yoshida, S., Sutton, P.J.H., Cancouët, R., Coatanoan, C., Dobbler, D., Juan,
A.G., Gourrion, J., Kolodziejczyk, N., Bernard, V., Bourlès, B., Claustre, H.,
1125 D’Ortenzio, F., Le Reste, S., Le Traon, P.Y., Rannou, J.P., Saout-Grit, C.,
Speich, S., Thierry, V., Verbrugge, N., Angel-Benavides, I.M., Klein, B., No-
tarstefano, G., Poulain, P.M., Vélez-Belchí, P., Suga, T., Ando, K., Iwasaka,
N., Kobayashi, T., Masuda, S., Oka, E., Sato, K., Nakamura, T., Sato, K.,
Takatsuki, Y., Yoshida, T., Cowley, R., Lovell, J.L., Oke, P.R., van Wijk,
1130 E.M., Carse, F., Donnelly, M., Gould, W.J., Gowers, K., King, B.A., Loch,
S.G., Mowat, M., Turton, J., Rama Rao, E.P., Ravichandran, M., Freeland,
H.J., Gaboury, I., Gilbert, D., Greenan, B.J.W., Ouellet, M., Ross, T., Tran,
A., Dong, M., Liu, Z., Xu, J., Kang, K., Jo, H., Kim, S.D., Park, H.M., 2020.
Argo data 1999–2019: Two million temperature-salinity profiles and subsur-
1135 face velocity observations from a global array of profiling floats. *Frontiers in*
Marine Science 7, 700. URL: [https://www.frontiersin.org/article/10.](https://www.frontiersin.org/article/10.3389/fmars.2020.00700)
3389/fmars.2020.00700, doi:10.3389/fmars.2020.00700.

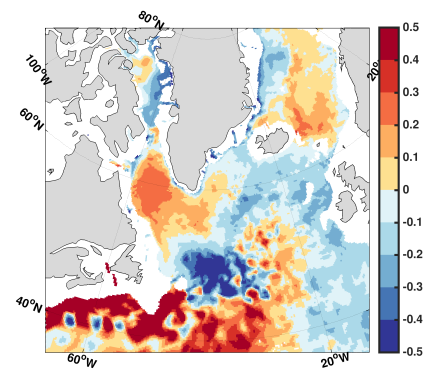
- Yashayaev, I., Loder, J.W., 2009. Enhanced production of Labrador Sea Water in 2008. *Geophysical Research Letters* 36. doi:10.1029/2008GL036162.
- 1140 Yashayaev, I., Loder, J.W., 2016. Recurrent replenishment of Labrador Sea Water and associated decadal-scale variability. *Journal of Geophysical Research: Oceans* 121, 8095–8114. URL: <https://agupubs.onlinelibrary.wiley.com/doi/abs/10.1002/2016JC012046>, doi:10.1002/2016JC012046, arXiv:<https://agupubs.onlinelibrary.wiley.com/doi/pdf/10.1002/2016JC012046>.
- 1145 Yashayaev, I., Loder, J.W., 2017. Further intensification of deep convection in the Labrador Sea in 2016. *Geophysical Research Letters* 44, 1429–1438. URL: <https://agupubs.onlinelibrary.wiley.com/doi/abs/10.1002/2016GL071668>, doi:10.1002/2016GL071668, arXiv:<https://agupubs.onlinelibrary.wiley.com/doi/pdf/10.1002/2016GL071668>.



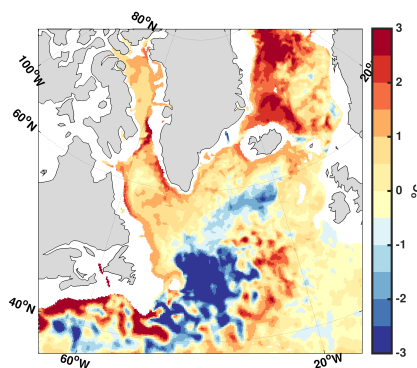
a. C50 Salinity



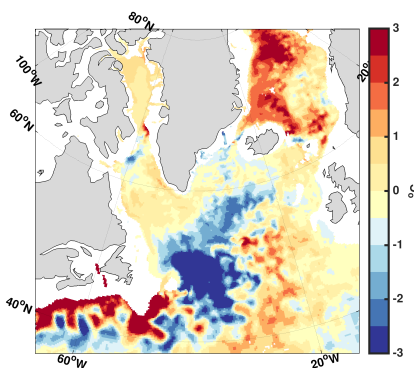
b. C75 Salinity



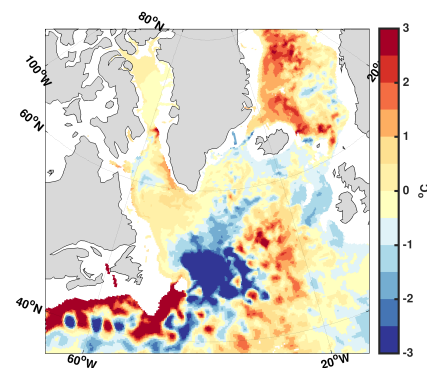
c. D75 Salinity



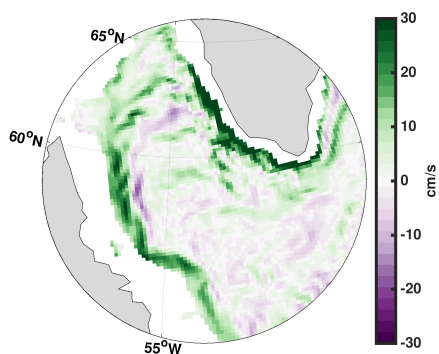
d. C50 Potential Temperature



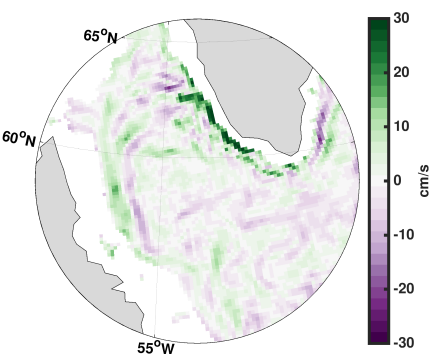
e. C75 Potential Temperature



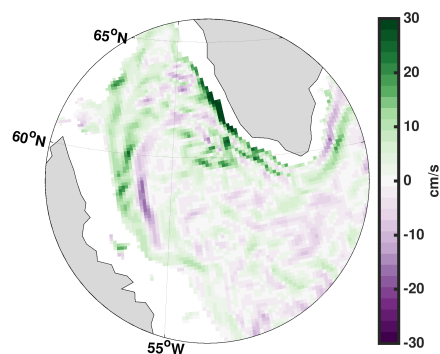
f. D75 Potential Temperature



g. C50 Velocity

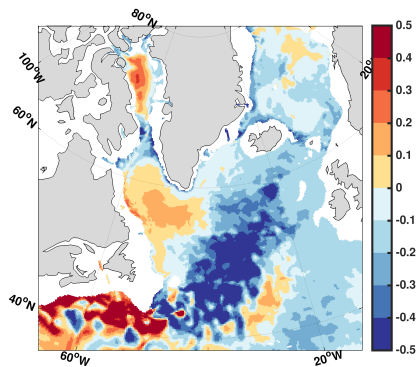


h. C75 Velocity

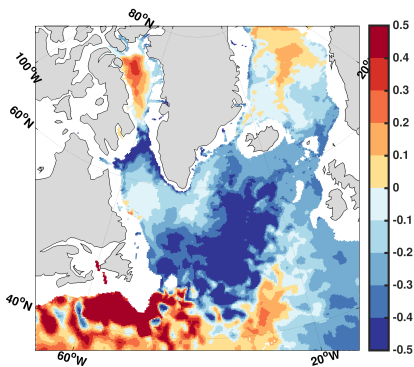


i. D75 Velocity

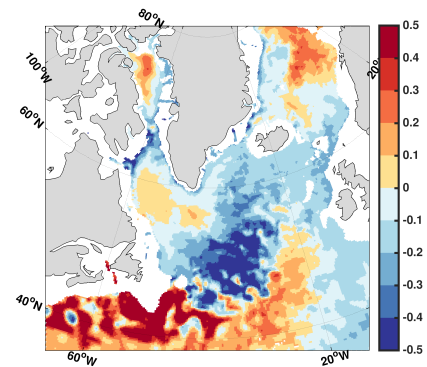
Figure S1: 2017 minus 2002 over the upper 450 m of the water column.



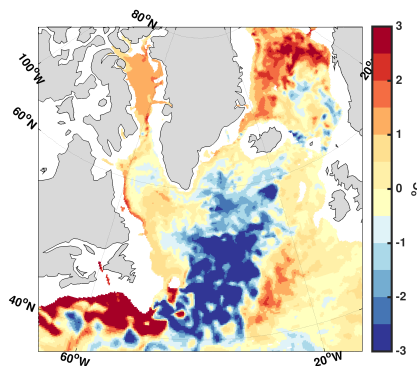
a. C50 Salinity



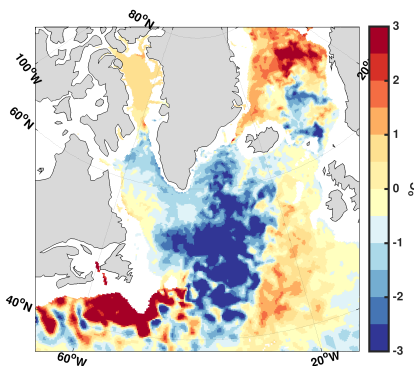
b. C75 Salinity



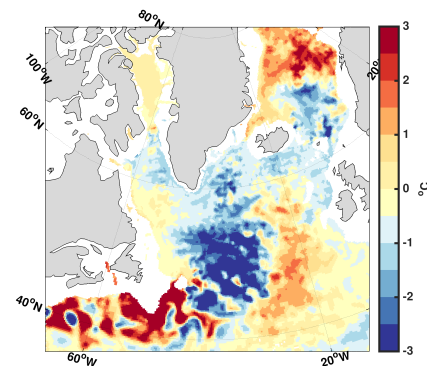
c. D75 Salinity



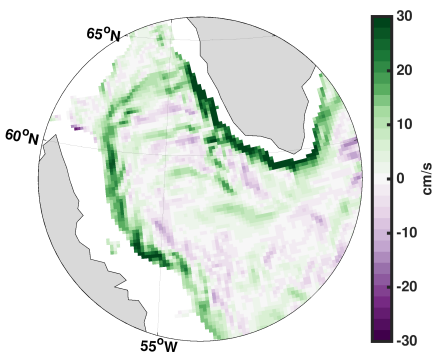
d. C50 Potential Temperature



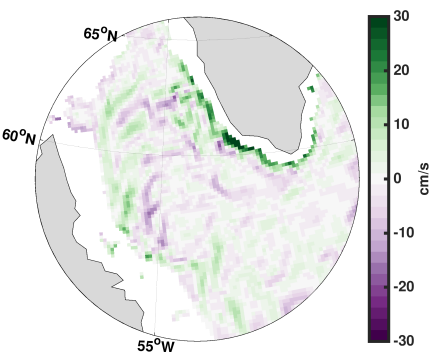
e. C75 Potential Temperature



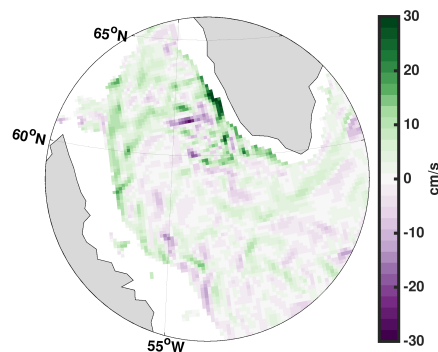
f. D75 Potential Temperature



g. C50 Velocity

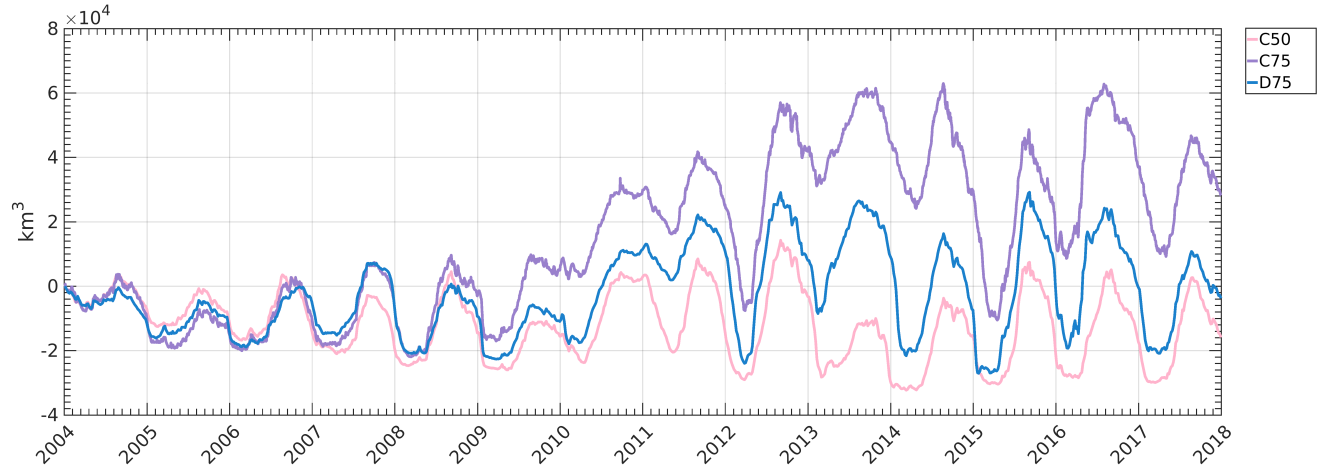


h. C75 Velocity

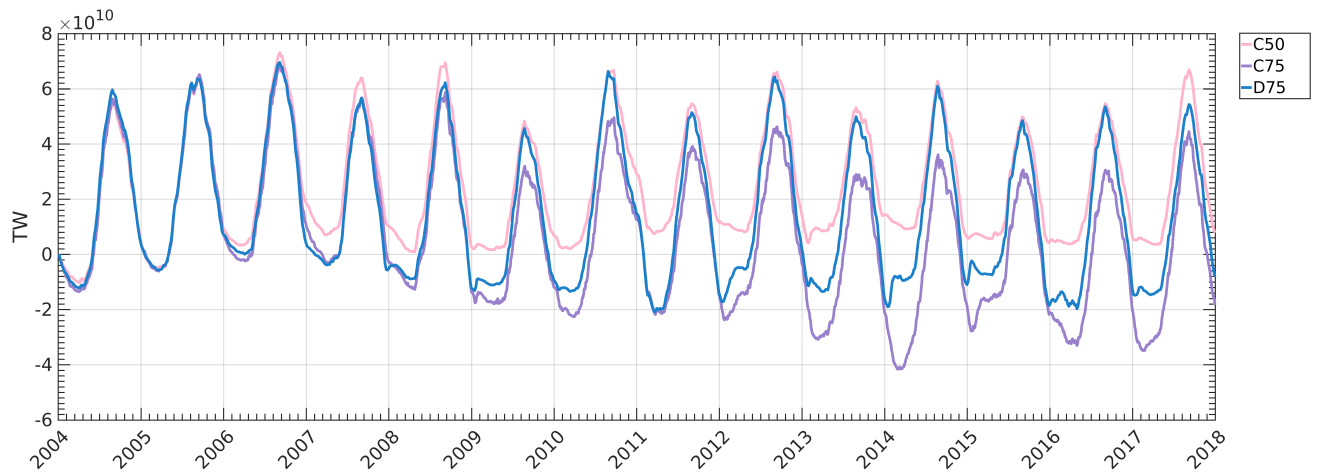


i. D75 Velocity

Figure S2: 2017 minus 2004 over the upper 450 m of the water column.



a. Freshwater Content



b. Heat Content

Figure S3: Interior of the Labrador Sea's freshwater (a) and heat content (b) over the top 1500 m of the water column (Equation 2 and Equation 3, but with $S_{ref} = 34.8$ (Aagaard and Carmack, 1989) and $T_{ref} = -2^{\circ}C$.). With a reference to the beginning of the time series; therefore, an anomaly from the start's state is shown (5 day average at the start of January 2004).

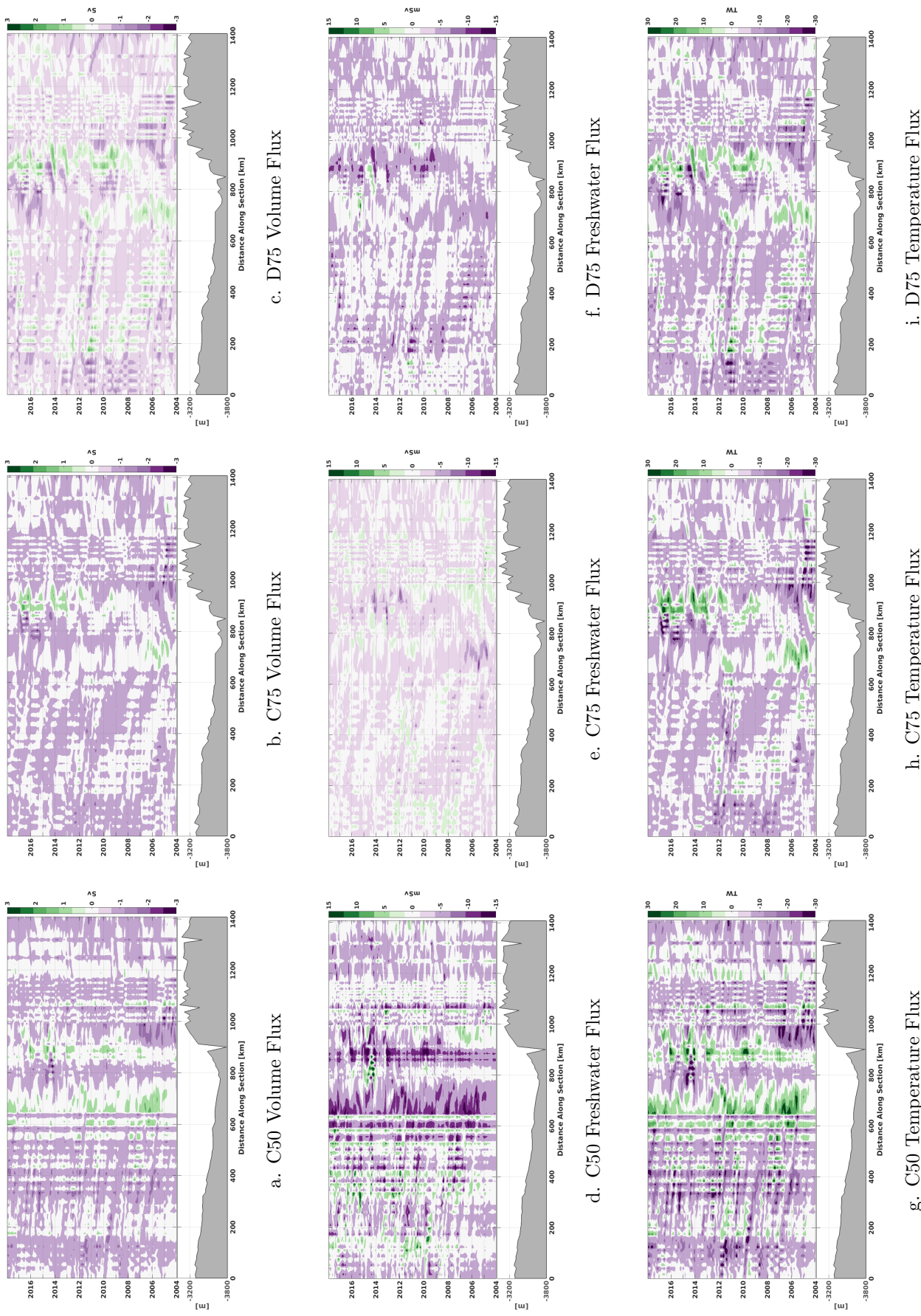


Figure S4: Monthly averaged fluxes into (positive) and out of (negative) the interior of the Labrador Sea (into and out-of the page, respectively). Fluxes are taken by the summation of the water column from 0 to 1500 m along the section using Equations 4 and 5. The reference salinity is $S_{ref} = 34.8$ (Aagaard and Carmack, 1989) and the reference temperature is $T_{ref} = 0^{\circ}C$. Distance markers along the section on the x-axis can be seen in Figure 1. A comparison of changing the vertical levels and atmospheric forcing is shown with C50 as the left column, C75 as the centre column, and D75 on the right column. Each row shows a different type of flux; the first row shows volume flux in Sv, the second row shows freshwater flux in mSv, and the third row shows temperature flux in TW.